

On the Influence of Swell Propagation Angle on Surface Drag

EDWARD G. PATTON, PETER P. SULLIVAN, BRANKO KOSOVIĆ, AND JIMY DUDHIA

National Center for Atmospheric Research, Boulder, Colorado

LARRY MAHRT

NorthWest Research Associates, Corvallis, Oregon

MARK ŽAGAR AND TOMISLAV MARIĆ

Vestas Wind Systems A/S, Arhaus, Denmark

(Manuscript received 11 August 2018, in final form 4 February 2019)

ABSTRACT

A combination of turbulence-resolving large-eddy simulations and observations are used to examine the influence of swell amplitude and swell propagation angle on surface drag. Based on the analysis a new surface roughness parameterization with nonequilibrium wave effects is proposed. The surface roughness accounts for swell amplitude and wavelength and its relative motion with respect to the mean wind direction. The proposed parameterization is tested in uncoupled three-dimensional Weather and Research Forecasting (WRF) simulations at grid sizes near 1 km where we explore potential implications of our modifications for two-way coupled atmosphere–wave models. Wind–wave misalignment likely explains the large scatter in observed nondimensional surface roughness under swell-dominated conditions. Andreas et al.’s relationship between friction velocity and the 10-m wind speed under predicts the increased drag produced by misaligned winds and waves. Incorporating wave-state (speed and direction) influences in parameterizations improves predictive skill. In a broad sense, these results suggest that one needs information on winds and wave state to upscale buoy measurements.


1. Introduction

It is well known that fluctuations in the turbulent atmosphere couple with the underlying water surface to grow surface waves (e.g., Phillips 1977), where the scale, phase, and speed of the wave field ultimately depends on the strength and mean wind direction. High winds in one location can generate large, rapidly traveling waves that can persist over extended periods and travel great distances such that at any given location, the current wave state is rarely in strict wind–wave equilibrium (e.g., Hanley et al. 2010). Wind–wave equilibrium is realized when winds blow with sufficient stationarity that the wave spectrum does not change with fetch (or distance from shore), that is, the wind

input is balanced by wave dissipation and nonlinear interactions in the wave action equation (e.g., Csanady 2001).

Recent observations (e.g., Grachev and Fairall 2001; Rutgersson et al. 2001; Smedman et al. 2009; Edson et al. 2013), turbulence closure modeling (e.g., Li et al. 2000; Hanley and Belcher 2008), and turbulence-resolving simulations (e.g., Sullivan et al. 2008, 2014) all show that these fast-moving water waves generated far from shore (i.e., swell) impact boundary layer winds by imparting an upward flux of momentum from the ocean to the atmosphere. Nonequilibrium waves modify the relationship between the surface and winds aloft. The marine atmospheric boundary layer typically exhibits much shallower depths than those occurring over land, particularly during daytime periods; hence, the character of the underlying surface is felt though a much greater percentage of the marine atmospheric boundary layer than of the atmospheric boundary layer over land.

Many models of wind–wave coupling rely on an equilibrium wind–wave assumption that is generally not achieved in coastal zones where future U.S. offshore

 Denotes content that is immediately available upon publication as open access.

Corresponding author: Edward G. Patton, patton@ucar.edu

turbine deployments are likely to be located (Hanley et al. 2010; Semedo et al. 2011). Coastal regions especially depart from wind–wave equilibrium due to 1) diurnal forcing associated with the daily sea breeze, 2) a shallow water column which limits wave growth, and 3) distant storms generating high-amplitude swell that arrives in coastal regions often dominating the local wave state.

Analysis of winds and turbulence over swell-dominated surfaces has generally underappreciated the nonlocal origin of swell and the frequent misalignment of the swell propagation direction with the wind. Geernaert (1988) and Geernaert et al. (1993) interrogated this question via observations in the North Sea and found that swell frequently travels in directions different from the wind and speculated this results in misaligned stress and wind vectors which has ramifications for applying Monin–Obukhov similarity theory (MOST). Larsén et al. (2003) found during weak winds that surface drag depends strongly on sea state and neglecting cross-swell effects leads to an underestimate of surface stress for periods with large ϕ (i.e., the angle between the mean 10-m wind direction and the propagation direction of the swell). How surface stress responds to misaligned surface waves and how to incorporate the atmospheric response in parameterizations remains unclear.

Marine atmospheric boundary layer parameterizations are currently used 1) to correlate buoy measurements with the wind and turbulence profiles aloft and 2) to represent the dynamical coupling between the overlying flow and the water surface in numerical weather prediction models. Current parameterizations do not account for the coupled influences of stratification and nonequilibrium wave states on the marine boundary layer structure. Recent studies (e.g., Tambke et al. 2005) show that parameterizations used to represent marine boundary layer winds/turbulence commonly result in a significant root-mean-square error (RMSE; $\sim 3 \text{ m s}^{-1}$ for a 48-h forecast). Substantial deviations from expected wind profile shapes were observed across a wide range of atmospheric stability conditions. Such errors indicate that current approaches to modeling the marine atmospheric boundary layer [i.e., those based on simple power law wind profile assumptions such as Wind Atlas Analysis and Application Program (WASP), or on MOST] do not accurately account for wind–wave coupling (Smedman et al. 2009). Power produced by wind turbines is proportional to wind speed cubed, and significant uncertainty in hub-height wind forecasts is not acceptable for operational use.

This paper uses a combination of turbulence-resolving large-eddy simulations (LESs) and observations to examine the atmospheric response under nonequilibrium wave states. The analysis illuminates the nonlinear coupling

between winds and waves, and this information is further used to modify the roughness model in an existing surface layer parameterization. The surface roughness modifications account for swell amplitude and wavelength and its relative motion with respect to the mean wind direction.

The open source WRF model (Skamarock et al. 2008) is widely used for wind resource analysis and forecasting and serves as a platform to test modifications to the Mellor–Yamada–Nakanishi–Niino (MYNN) boundary layer parameterization (Nakanishi and Niino 2004) incorporating wave effects. The newly implemented parameterization is tested in three-dimensional WRF simulations at grid sizes near 1 km to identify the parameterization's impact on simulated atmospheric boundary layer (ABL)-scale winds at mesoscale resolutions.

2. FINO1 observations

a. Data description

Since 2003, FuE-Zentrum FH Kiel GmbH (2013) has collected nearly continuous observations at Forschungsplattformen in Nord- und Ostsee Nr. 1 (FINO1) located 45 km north of Borkum Island, Germany ($54^{\circ}0'53.5''\text{N}$, $6^{\circ}35'15.5''\text{E}$). The water depth at FINO1 is ~ 30 m. Wind speed is measured at eight levels using Vector Instruments cup anemometers sampled at 1 Hz at heights ranging from 34 to 101 m above sea level. Wind direction is measured with Adolf Thies GmbH and Co. KG wind vanes at four levels from 34 to 91.5 m above the sea surface. The cup anemometer booms face southeast, and three additional sonic anemometer booms face northwest measuring three wind velocity components at 30, 50, and 70 m, so unobstructed wind speed measurements can be constructed under a wide range of wind directions. The booms holding the instrumentation range in length from 3 to 6.5 m in an attempt to mitigate the impact of the somewhat bulky FINO1 tower infrastructure. Comparisons between lidar measurements (a Leosphere Windcube WL07) and the cup anemometers over a full year at FINO1 demonstrate that if one excludes wind directions between 290° and 350° then the lidar and cup anemometer measurements show high correlation with R^2 values higher than 0.99 for both speed and direction (Westerhellweg et al. 2010). For the other wind sectors, Westerhellweg et al. (2012) applied a “Uniform Ambient Flow” method to derive functions correcting for potential tower-infrastructure-induced pressure forces that could impact the observations; the amplitude of these corrections is small—falling between 2% and 4% or smaller, which is well within the range of calibration uncertainty. We are therefore reasonably confident that the tower infrastructure does

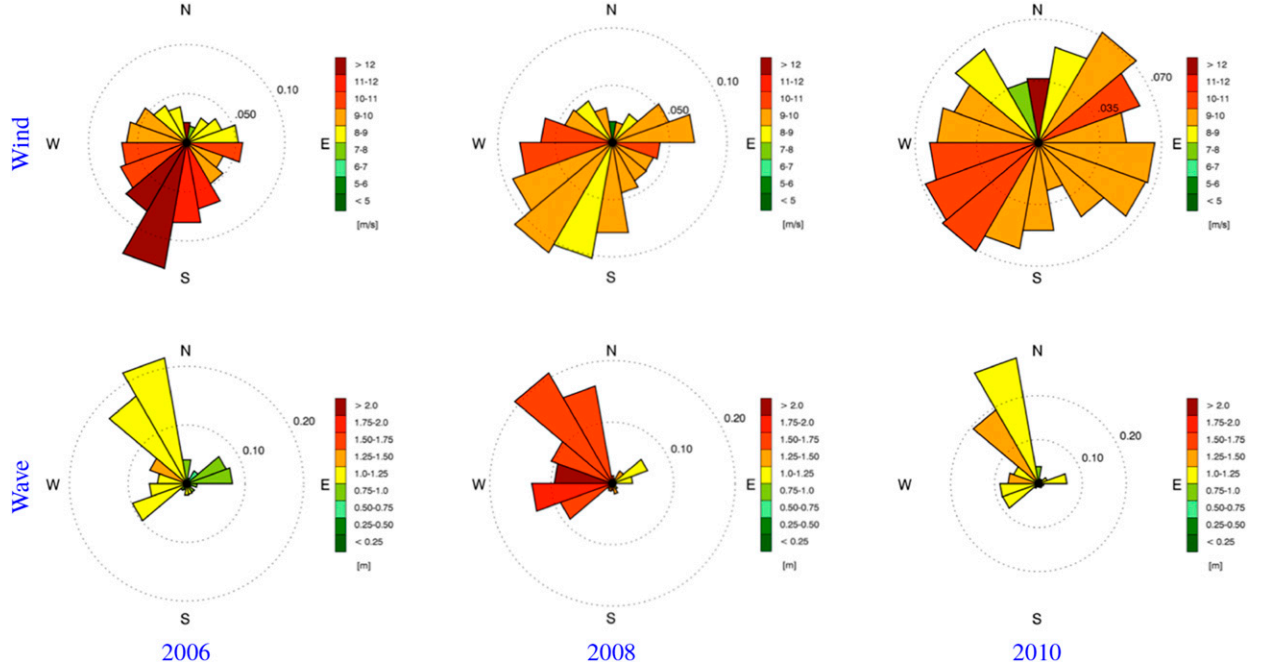


FIG. 1. (top) Wind and (bottom) wave roses at FINO1 for (left) 2006, (center) 2008, and (right) 2010.

not significantly impact the wind profile observations used in our study.

Hourly measurements of significant wave height, mean wave direction, and peak wave direction located at $54^{\circ}0'51''\text{N}$, $6^{\circ}35'11''\text{E}$ are collected using a Nortek Acoustic Wave and Current (AWAC) meter mounted on the sea floor. Bundesamt für Seeschifffahrt und Hydrographie (2016) describes further sensor information for FINO1. Data from the FINO1 tower serve both to motivate the analysis of swell-propagation direction influence on surface drag and as a dataset to evaluate the impact of a new parameterization.

b. Winds and waves climatology

Analysis of the dominant wind directions and wind speeds at FINO1 (Fig. 1) shows that winds are generally from the southwest, but can come from any direction. However, surface waves generally propagate from the northwest with an average significant wave height between 1.25 and 1.75 m. Winds and waves at FINO1 are therefore rarely aligned and are rarely in equilibrium with each other, making it an ideal dataset for our intended use.

3. Turbulence resolving simulation

a. The atmospheric LES

Explicit details outlining our computational technique can be found in Sullivan et al. (2014). In basic terms, our

LES model with a flat boundary Sullivan and Patton (2011) is adapted to the situation with a three-dimensional time-dependent lower boundary with shape $h = h(x, y, t)$ by applying a transformation to the equations in physical space coordinates $\mathbf{x} = x_i = (x, y, z)$ that maps them onto computational coordinates $\boldsymbol{\xi} = \xi_i = (\xi, \eta, \zeta)$. The computational mesh in physical space is surface following, nonorthogonal, and time varying. Vertical grid lines are held fixed at a particular (x, y) location on the surface but translate vertically as a function of time t . In order for the scheme to be conservative, the grid movement satisfies the geometric conservation law (e.g., Thomas and Lombard 1979).

The primary equation set includes a mass conservation (continuity) equation, Boussinesq equations for momentum $\mathbf{u} = u_i = (u, v, w)$ transport, a transport equation for potential temperature θ , a subfilter-scale energy e equation, and a Poisson equation for pressure p^* . Momentum and scalar advection are written in flux-conserving form using a contravariant flux velocity:

$$U_i = \frac{u_j}{J} \frac{\partial \xi_j}{\partial x_i}, \quad (1)$$

where J is the Jacobian, and $\mathbf{U} = U_i = (U, V, W)$ are normal to a constant ξ_j surface. Explicit filtering of the equations generates subfilter-scale stresses T_{ij} , which are parameterized using Deardorff's (1972) turbulent eddy viscosity approach. The momentum equations include

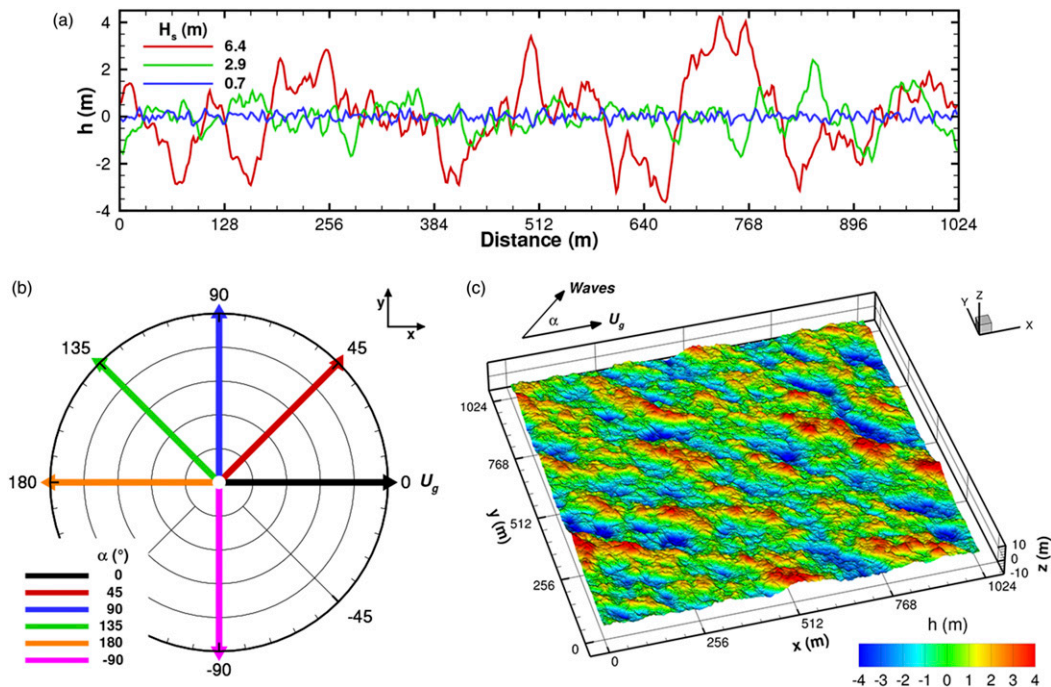


FIG. 2. (a) An instantaneous snapshot depicting the x variation at a fixed y location of the wavy surface h generated assuming wind–wave equilibrium and imposing three unique 10-m wind speeds $U_{10} = (15, 10, 5) \text{ m s}^{-1}$. Each configuration therefore produces waves with a significant wave height $H_s \sim 4\sigma_h = (6.4, 2.9, 0.7) \text{ m}$, respectively. (b) Polar plot looking down from above outlining the wave propagation directions for the six simulation configurations. For reference, the pressure gradient driving the flow (U_g) is oriented in the positive x direction (toward 0° , from left to right) in all simulations. The colored arrows show the wave’s propagation direction relative to U_g . So in the 0° case the waves are propagating in the same direction as the pressure gradient and are opposite the pressure gradient in the 180° case. (c) An example instantaneous surface [i.e., $h(x, y)$ at a single time t] where the waves (with $H_s = 6.4 \text{ m}$) propagate at a 45° angle relative to the geostrophic wind U_g , i.e., $\alpha = 45^\circ$.

buoyancy, Coriolis, and imposed pressure gradient forces.

The underlying surface is presumed fully rough such that a bulk aerodynamic formulation relates horizontal velocities at the lowest model level to the surface stress using an imposed bulk roughness z_o . No attempt has been made to account for spatially varying wind-generated unresolved surface roughness (e.g., Yang et al. 2013). To ensure no flow through (normal to) the water surface, the contravariant vertical velocity W at the lower boundary matches the time-derivative of the underlying surface shape h_t . Horizontal boundary conditions are periodic, and the upper boundary condition assumes Neumann conditions for all variables except for W and e , which are set to zero using Dirichlet conditions ensuring no momentum or scalar flux across the upper boundary.

b. The time-varying wavy surface

In terms of wave age, wind–wave equilibrium is empirically determined as $w_{\text{age}} = C_p/U_{10} = 1.2$, where U_{10} is a 10-m wind speed and C_p is the phase speed of the surface waves at the spectral peak. Thus nonequilibrium

swell $C_p/U_{10} > 1.2$ can be created in at least two ways. For example, 1) remotely generated waves with long wavelength (fast waves with large C_p) can propagate into a region with locally weak winds, or 2) starting from wind–wave equilibrium the U_{10} wind can abruptly decrease or shift direction. Nature does both. A general model of remotely generated swell is not possible as it is specific to the source, as well as the propagation distance and direction. In our study, we have instead chosen to create nonequilibrium swell using the second way, that is, we vary wave age by varying U_{10} while holding C_p (or the wave field) fixed.

The surface waves are built offline following Donelan’s empirical directional spectrum (Donelan et al. 1985; Komen et al. 1994) using 1) an assumption that the wave field is a sum of linear plane waves with random phase and 2) an assumption of wind–wave equilibrium. Surface waves are generated using three different U_{10} values: $(15, 10, 5) \text{ m s}^{-1}$. These U_{10} modifications result in waves with C_p values $(18, 12, 6) \text{ m s}^{-1}$ and which produce waves with significant wave heights $H_s = (6.4, 2.9, 0.7) \text{ m}$; using the root-mean-square elevation σ_h , $H_s = 4\sigma_h$. See Figs. 2a and 2c for an example. Note that the waves in

these simulations are time- and spatially evolving, but are externally imposed and therefore do not respond to local wind forcing.

For each of these three wavy surfaces, six simulations are performed to investigate the impact of the wave propagation direction relative to the geostrophic wind direction; where the propagation angle varies from (0° , 45° , 90° , 135° , 180° , and -90°) relative to the direction of the geostrophic wind forcing. [Figures 2b and 2c](#) present a schematic and example surface.

c. The simulation strategy

To generate the simulations, the NCAR large-eddy simulation code ([Sullivan et al. 2014](#)) is first configured to represent flow over a completely flat but aerodynamically rough surface (with a roughness length $z_o = 2 \times 10^{-4}$ m). The domain is $1024 \times 1024 \times 512$ m³, resolved by $512 \times 512 \times 128$ grid points. The vertical coordinate uses an algebraic stretching strategy allowing fine resolution near the surface (~ 0.25 m) decaying with height (to ~ 13 m at domain top). The simulations are presumed to take place at approximately 45° N latitude where the Coriolis parameter $f = 1 \times 10^{-4}$ s⁻¹. The initial virtual potential temperature profile is constant at 290 K throughout the lowest 100 m, above which the profile increases at a rate of 3 K km⁻¹.

Turbulence in the flat-domain simulations is initiated by placing randomly distributed divergence-free fluctuations on the horizontal velocity and temperature fields and imposing a small horizontally homogeneous surface buoyancy flux (10 W m⁻²) for the first 20 000 time steps (approximately 1800 s). After these initial 20 000 time steps, the surface buoyancy flux is set to 0 W m⁻², that is, the water surface temperature matches the air temperature, and the solutions are integrated forward for an additional 80 000 time steps (or a total of approximately 2.5 h) to allow the buoyancy influences to dissipate and for the turbulence to reach equilibrium with the imposed forcing. At this time, a flat-domain dataset is saved.

Most of the wavy simulations are initiated from this flat-domain dataset that was generated using a geostrophic wind forcing of $\mathbf{U}_g = (U_g, V_g) = (10, 0)$ m s⁻¹. To expand the investigation across sufficient wave age and stability, two additional flat-domain simulations were conducted: 1) another near-neutral stability simulation, but with $\mathbf{U}_g = (5, 0)$ m s⁻¹, and 2) another using the original $\mathbf{U}_g = (10, 0)$ m s⁻¹ geostrophic wind forcing, but where the sea surface temperature is cooled at a rate of 0.25 K h⁻¹ (similar to [Beare et al. 2006](#)).

For each H_s and α simulated, the waves are gradually grown into the flat-domain flow fields over a period of 400 s and each of the simulations are integrated forward

for an additional $1\text{--}2 \times 10^5$ time steps. Due to the rapidly varying underlying surface, the time steps decrease such that the wavy simulations are integrated over approximately 1.5–2 h of simulated time. [Table 1](#) outlines the simulations conducted. In a broad sense, these simulations interrogate what happens to drag, roughness, and flow patterns for a sudden change in the wind for an imposed set of waves. Thus, in our problem posing we start from a well-known initial wind–wave spectrum given by [Donelan et al.'s \(1985\)](#) empirical formulas and generate nonequilibrium conditions by varying wind speed and direction.

4. Results

a. Influence of wind-wave alignment

In this section, we focus our attention on a single set of six simulations (cases A1–A6). These simulations are all driven by the same geostrophic winds ($\mathbf{U}_g = [10, 0]$ m s⁻¹), interact with a wavy surface where $H_s = 6.4$ m. The primary variation between these simulations results from the wavy surface propagating at six different angles (0° , 45° , 90° , 135° , 180° , -90°) relative to the direction of the geostrophic wind forcing. Bulk characteristics of these simulations can be found in the first six rows of [Table 1](#).

1) INSTANTANEOUS WIND FIELDS

To gain an initial appreciation for the impact of the wavy surface's propagation direction, [Fig. 3](#) presents instantaneous vertical slices of streamwise velocity for two simulations whose forcing is otherwise identical (i.e., $U_g = 10$ m s⁻¹, $H_s = 6.4$ m), but the waves propagate at $\alpha = 0^\circ$ (case A1) and 180° (case A5). Compared to $\alpha = 0^\circ$, flow over winds/waves with $\alpha = 180^\circ$ reveals notably lower streamwise velocity throughout the ABL with much larger horizontal variability. Statistics quantifying these variations and a discussion of the mechanisms producing these variations follows shortly.

Horizontal surfaces of instantaneous streamwise velocity fluctuations at $\zeta \approx 5$ m above the water surface ([Fig. 4](#)) depict substantial modulation of the streamwise velocity field by surface waves. All four simulations are responding to an identical and imposed geostrophic forcing \mathbf{U}_g aligned with the x direction. In [Figs. 4a and 4c](#) (and again in [Figs. 4b and 4d](#)), the waves are oriented similarly with each other, but between the two panels the waves propagate in opposite directions. In [Fig. 4a](#), the waves travel from left to right ($\alpha = 0^\circ$, case A1), and in [Fig. 4c](#) they travel from right to left ($\alpha = 180^\circ$, case A5); while in [Fig. 4b](#) the waves travel from bottom to top

TABLE 1. Table outlining key characteristics of the large-eddy simulation cases under investigation. The first column defines case names that will be used when discussing the simulations. Here, U_g is the imposed geostrophic wind component in the x direction ($V_g = 0 \text{ m s}^{-1}$ for all cases); the significant wave height H_s is calculated as $4\sigma_h$; α is the wave-propagation angle relative to the geostrophic wind direction in degrees; $\partial T_s/\partial t$ is the imposed surface cooling rate; w_{age} is the wave age calculated as C_p/U_a , where $U_a = |\langle \mathbf{u}_a \rangle|$; Ω is the angle between U_a and the geostrophic wind vector \mathbf{U}_g in radians, and ϕ is the angle between U_a and the wave-propagation direction in radians; $u_{*,s}$ is the friction velocity evaluated at the surface, and $u_{*,a}$ is the friction velocity evaluated at $\zeta_a = 10 \text{ m}$ [see Eq. (3)]; τ_{p_x} and τ_{p_y} represent the contribution of pressure drag to the total momentum stress at the surface in a coordinate system aligned with \mathbf{U}_g , respectively; z_i is the horizontal- and time-averaged boundary layer depth defined as the height of the maximum potential temperature gradient; and L is the Monin–Obukhov length evaluated at ζ_a .

	Imposed				Result									
	U_g (m s^{-1})	H_s (m)	α ($^\circ$)	$\partial T_s/\partial t$ (K h^{-1})	w_{age}	Ω (rad)	ϕ (rad)	U_a (m s^{-1})	$u_{*,s}$ (m s^{-1})	$u_{*,a}$ (m s^{-1})	τ_{p_x} ($\text{m}^2 \text{ s}^{-2}$)	τ_{p_y} ($\text{m}^2 \text{ s}^{-2}$)	z_i (m)	z_i/L
A1	10	6.4	0	0	2.99	0.27	-0.27	6.02	0.22	0.22	0.009	-0.018	301.0	0.30
A2	10	6.4	45	0	2.97	0.31	0.48	6.06	0.22	0.22	-0.132	0.039	300.6	0.30
A3	10	6.4	90	0	2.95	0.38	1.12	6.10	0.24	0.25	-0.051	0.108	306.1	0.31
A4	10	6.4	135	0	3.23	0.47	1.89	5.58	0.25	0.33	-0.117	0.073	318.1	0.32
A5	10	6.4	180	0	3.85	0.35	2.79	4.68	0.23	0.39	-0.136	-0.008	333.4	0.33
A6	10	6.4	-90	0	3.28	0.09	-1.66	5.49	0.24	0.29	-0.040	-0.143	305.1	0.31
B1	10	2.9	0	0	1.97	0.29	-0.29	6.10	0.22	0.23	-0.017	-0.008	309.4	0.31
B2	10	2.9	45	0	1.96	0.31	0.48	6.13	0.22	0.23	-0.017	0.002	309.5	0.31
B3	10	2.9	90	0	1.95	0.38	1.20	6.15	0.23	0.24	-0.028	0.044	315.2	0.32
B4	10	2.9	135	0	2.13	0.46	1.89	5.64	0.23	0.29	-0.073	0.044	323.4	0.32
B5	10	2.9	180	0	2.47	0.38	2.76	4.87	0.20	0.34	-0.094	-0.006	334.8	0.34
B6	10	2.9	-90	0	2.15	0.15	-1.72	5.57	0.22	0.27	-0.024	-0.082	313.0	0.31
C1	10	0.7	0	0	0.97	0.32	-0.32	6.18	0.23	0.23	-0.006	-0.001	317.6	0.32
C2	10	0.7	45	0	0.97	0.32	0.47	6.21	0.23	0.23	-0.005	-0.003	317.8	0.32
C3	10	0.7	90	0	0.96	0.35	1.22	6.26	0.23	0.23	-0.003	0.001	318.3	0.32
C4	10	0.7	135	0	0.99	0.40	1.96	6.02	0.22	0.25	-0.009	0.006	324.1	0.32
C5	10	0.7	180	0	1.08	0.37	2.77	5.54	0.21	0.28	-0.014	-0.001	332.2	0.33
C6	10	0.7	-90	0	1.02	0.25	-1.82	5.91	0.22	0.24	-0.003	-0.009	317.8	0.32
D1	5	6.4	0	0	4.93	0.31	-0.31	3.66	0.16	0.09	0.452	-0.009	206.2	0.21
D2	5	6.4	45	0	4.83	0.44	0.34	3.73	0.16	0.10	0.201	0.321	205.8	0.21
D3	5	6.4	90	0	4.94	0.56	1.01	3.65	0.17	0.16	-0.007	0.284	207.0	0.21
D4	5	6.4	135	0	5.74	0.67	1.68	3.13	0.18	0.23	-0.177	0.127	215.9	0.22
D5	5	6.4	180	0	7.91	0.56	2.58	2.28	0.16	0.28	-0.188	-0.001	227.5	0.23
D6	5	6.4	-90	0	6.10	0.02	-1.59	2.95	0.17	0.21	-0.004	-0.238	206.9	0.21
E1	10	6.4	0	0.25	2.84	0.38	-0.38	6.34	0.18	0.18	0.018	-0.038	185.4	4.09
E3	10	6.4	90	0.25	2.78	0.53	1.04	6.47	0.21	0.21	-0.077	0.115	188.1	3.47
E5	10	6.4	180	0.25	4.86	0.79	2.36	3.71	0.19	0.30	-0.183	-0.018	213.8	7.65
E6	10	6.4	-90	0.25	3.82	0.06	-1.63	4.71	0.19	0.23	-0.056	-0.218	185.6	4.72

($\alpha = 90^\circ$, case A3), and in Fig. 4d they travel from top to bottom ($\alpha = -90^\circ$, case A6). Apparent in these slices is that wave-propagation direction directly impacts spatial character and magnitude of velocity fluctuations at $\zeta \approx 5 \text{ m}$.

2) ATMOSPHERIC BOUNDARY LAYER DEPTH

The depth of the ABL represents an integral measure of all the turbulent motions produced and dissipated in the ABL through interactions with the surface. Therefore, evolution of the ABL depth occurring under variations in a single parameter illustrates that parameter's bulk influence on ABL turbulence.

Following Sullivan et al. (1998) and Davis et al. (2000), the ABL depth can be determined by searching vertically through an instantaneous volume of

simulated data for the height of the maximum vertical temperature gradient at every horizontal grid point. Following this search, one obtains height of the undulating surface coincident with the temperature inversion constraining ABL motions which can then be horizontally averaged to determine the average ABL depth at any instant in time. Time series of the instantaneous horizontally averaged ABL depth (Fig. 5) reveals that the wave-propagation direction influences the ABL growth rate.

Starting at wave-propagation directions α between 45° and 90° (cases A2 and A3), the ABL grows faster than for the case where the waves propagate in the same direction as the driving pressure gradient (i.e., $\alpha = 0^\circ$, case A1). The ABL growth rate increases in a systematic fashion toward a maximum growth rate

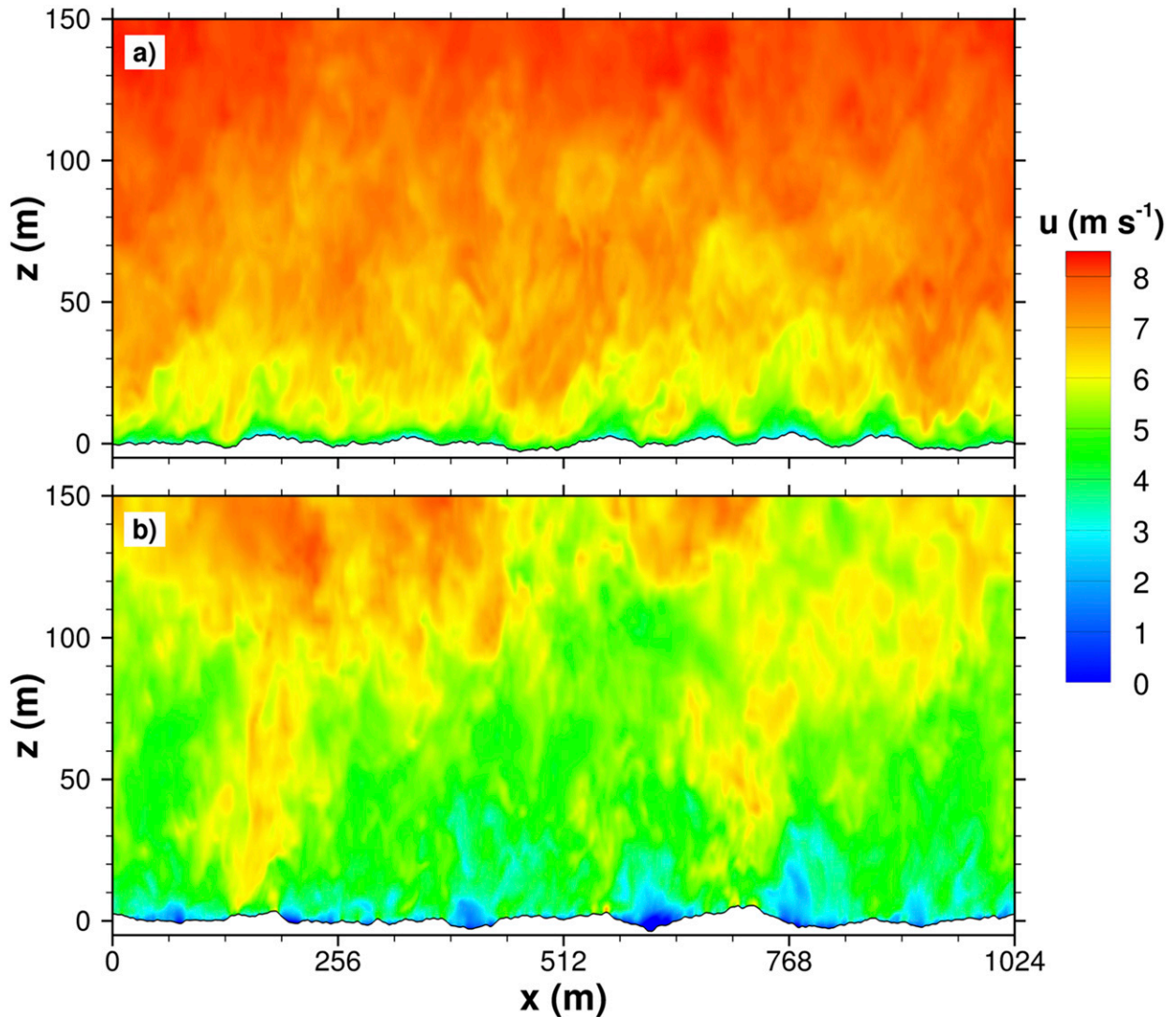


FIG. 3. Instantaneous vertical slices of streamwise wind velocity from two simulations where $\mathbf{U}_g = (10, 0) \text{ m s}^{-1}$ and $H_s = 6.4 \text{ m}$ for both cases. (a) For $\alpha = 0^\circ$ (case A1, waves propagating with the wind), and (b) for $\alpha = 180^\circ$ (case A5, waves propagating against the wind). The scales are the same between the two figures. Only the lowest 150 m of the domain is presented.

when the waves propagate in the opposite direction of the pressure gradient (i.e., 180° , case A5). The ABL growth rate responds similarly to waves propagating at $\alpha = \pm 90^\circ$ (cases A3 and A6).

3) DATA PROCESSING AND NORMALIZATION

Following Sullivan et al. (2014), statistics are calculated by averaging instantaneous quantities along ξ - η coordinate surfaces (i.e., along surfaces of constant ζ). Horizontal averaging in a wave-following coordinate system takes advantage of the periodic boundary conditions and allows for computing statistics down beneath the wave crests. These horizontally averaged vertical profiles are then additionally averaged in time.

Because the boundary layer grows at different rates across the simulations (e.g., Fig. 5), time averaging begins after 12 000 s of simulated time (when the flow has reached equilibrium with the underlying surface) and continues until the end of the simulation, where the instantaneous statistics are averaged into a time-evolving vertical coordinate system scaled by the instantaneous horizontally averaged z_i . The combination of the horizontal- and time-averaging processes is denoted by angle brackets, that is, $\langle \rangle$.

To enable comparison with field observations (e.g., Fairall et al. 2003; Edson et al. 2007) and following Sullivan et al. (2014), we adopt the friction velocity evaluated at a height $\zeta_a = 10 \text{ m}$ above the water surface

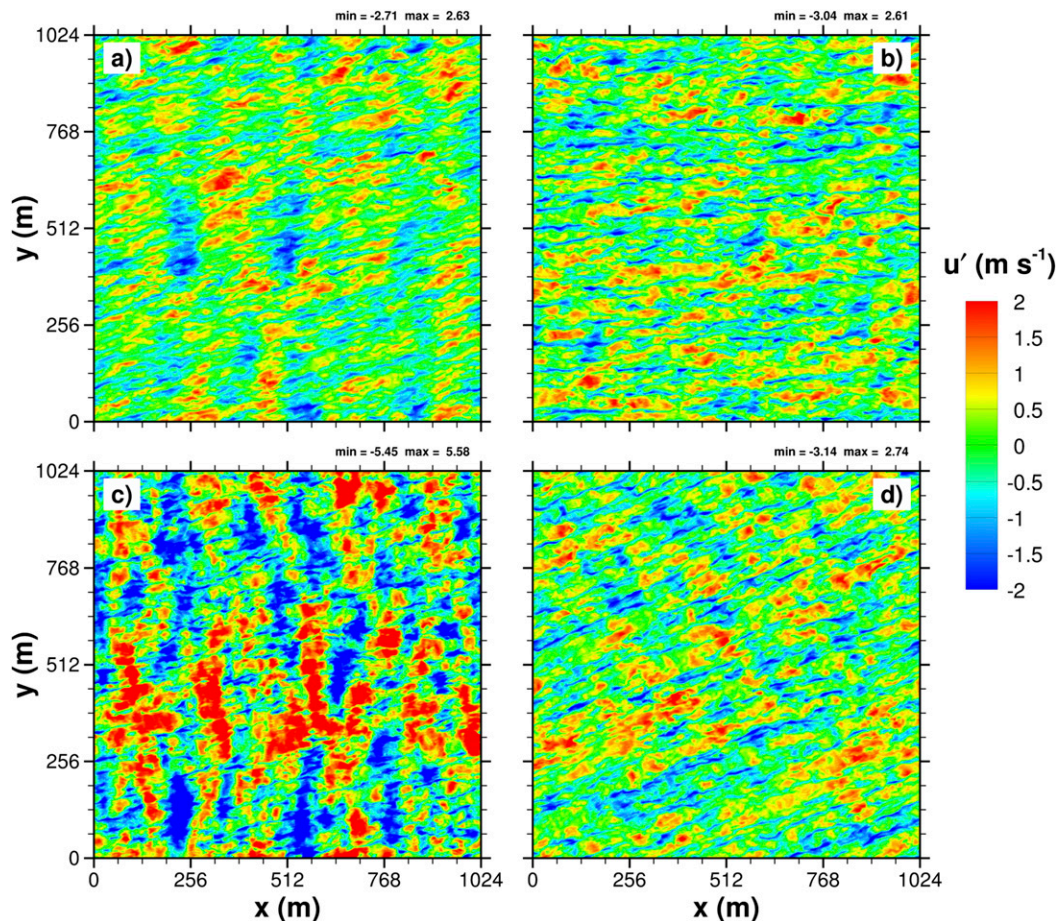


FIG. 4. Instantaneous horizontal surfaces of streamwise wind velocity fluctuations (i.e., deviations from the instantaneous average over an ξ - η surface) at a height of approximately 5 m from four simulations where $\mathbf{U}_g = (10, 0) \text{ m s}^{-1}$ and $H_s = 6.4 \text{ m}$ for all cases. The four panels present results for simulations with waves propagating in the: (a) $\alpha = 0^\circ$ (case A1), (b) $\alpha = 90^\circ$ (case A3), (c) $\alpha = 180^\circ$ (case A5), and (d) $\alpha = -90^\circ$ (case A6) directions. Here, \mathbf{U}_g is aligned with the x direction.

$u_{*,a}$ as our characteristic velocity scale. To obtain $u_{*,a}$, we first compute the vertical momentum stresses $\tau_{T,a} = (\tau_{T_x,a}, \tau_{T_y,a})$ at ζ_a :

$$\tau_{T_x,a} = \left\langle u(W - z_t) + \frac{T_{1k}}{J} \frac{\partial \zeta}{\partial x_k} + \frac{p^*}{J} \frac{\partial \zeta}{\partial x} \right\rangle_a, \quad (2a)$$

$$\tau_{T_y,a} = \left\langle \underbrace{v(W - z_t)}_{\tau_r} + \underbrace{\frac{T_{2k}}{J} \frac{\partial \zeta}{\partial x_k}}_{\tau_s} + \underbrace{\frac{p^*}{J} \frac{\partial \zeta}{\partial y}}_{\tau_p} \right\rangle_a, \quad (2b)$$

where z_t is the vertical grid speed. Each of the vector components includes contributions to the momentum stress from: 1) the resolved turbulence τ_r , 2) the subfilter-scale model τ_s , and 3) pressure-wave slope correlations τ_p , which account for vertical variations of the ξ - η surface

in physical space. For simplicity, when discussing momentum stresses in subsequent discussion not necessarily at a height of ζ_a , we will refer to the combination of resolved and subfilter-scale contributions to the stress as τ_r , that is, the total turbulent momentum stress $\tau_t = \tau_r + \tau_s$, and a subscript x or y will refer to the x or y component of the stress. From Eq. (2), we define a friction velocity at ζ_a as

$$u_{*,a} = |\tau_{T,a}|^{1/2}. \quad (3)$$

It is important to note that $u_{*,a}^2$ is not necessarily the same as the force at the water surface, which for these simulations is $u_{*,s}^2$ [calculated by evaluating Eqs. (2) and (3) at the water surface]. Figure 6 demonstrates the differences between $u_{*,a}$ and $u_{*,s}$; the actual values from each simulation are included in Table 1, and the mechanisms responsible for those differences will be discussed in section 5.

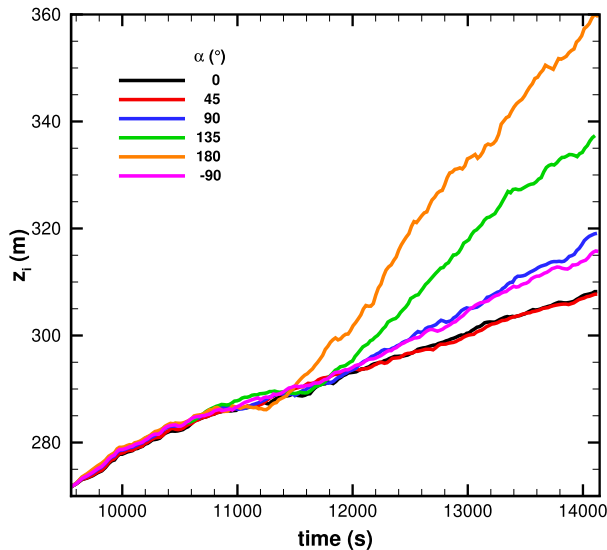


FIG. 5. Time evolution of the depth of the boundary layer z_i in response to swell ($H_s = 6.4$ m) propagating at specified angles α relative to the imposed geostrophic wind forcing ($\mathbf{U}_g = [10, 0]$ m s $^{-1}$); cases A1–A6. For all simulations, the waves begin to grow into the domain at 9555.46 s of simulated time and are at full amplitude 400 s later. Note that after ~ 1500 – 2000 s, the winds come into equilibrium with the underlying wavy surface as exhibited by the nearly constant boundary layer growth rates differing by wave angle α .

Wave age characterizes the wave propagation speed relative to the overlying atmospheric flow fields (e.g., Csanady 2001), and can be defined as $w_{\text{age}} = C_p/U_a$, where C_p is imposed by the three different wavy surfaces. Weaker wind regimes (i.e., increased wave age, open symbols) and wave-propagation direction (α , colors) produce the most dramatic differences between $u_{*,a}$ and $u_{*,s}$, where increased w_{age} reduces $u_{*,a}$ compared to $u_{*,s}$ for wave-following regimes, and in wave-opposing regimes $u_{*,a}$ increases compared to $u_{*,s}$ for all configurations.

4) MEAN WIND PROFILES

For these near-neutral¹ simulations, intercomparisons of the mean wind fields reveal that swell-propagation direction significantly affects horizontally and time-averaged wind speeds to heights all the way through the ABL (Fig. 7). With a fixed pressure gradient ($\mathbf{U}_g = [10, 0]$ m s $^{-1}$), the streamwise wind speeds $\langle u \rangle$ diminish as the swell propagation direction steps from 0° to 90° to a maximum wind speed decrease at 180° . Near the surface, lateral wind speeds $\langle v \rangle$ increase as the wave-propagation

¹ We use the term *near-neutral* somewhat loosely. Even though the surface buoyancy flux is 0 W m $^{-2}$, warm air is continually entrained at the top of the ABL making the flow *weakly stable*; see z_i/L in Table 1.

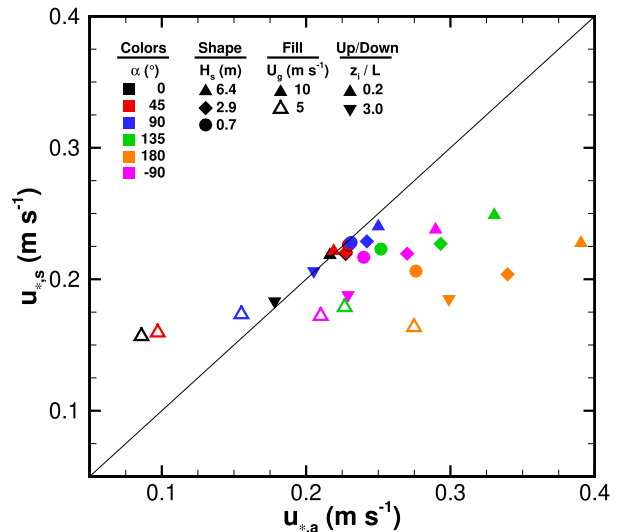


FIG. 6. Scatterplot demonstrating the relationship between $u_{*,a}$ and the surface friction velocity $u_{*,s}$ for all the simulations. The actual $u_{*,a}$ and $u_{*,s}$ values can be found in Table 1. The LES results are colored by α (the angle between the wave propagation direction and the geostrophic forcing direction). Each of these angles is presented for three different significant wave heights H_s and for a geostrophic wind of 10 m s $^{-1}$. For the largest/fastest waves ($H_s = 6.4$ m, $C_p = 18$ m s $^{-1}$), the open symbols represent LES results for a geostrophic wind of 5 m s $^{-1}$. The upward vs downward pointing triangles depict variations with atmospheric stability z_i/L . The thin black line marks the 1:1 line.

angle rotates from 0° to 90° ; $\langle v \rangle$ then decreases between $\alpha = 135^\circ$ and 180° , and dramatically reduces in magnitude for the -90° case as swell generates near-surface winds in the negative y direction.

Wave-propagation angles of $\pm 90^\circ$ reveal distinctly different wind profile responses (Fig. 7) because the simulations are conducted in the Northern Hemisphere and geostrophic balance ensures that the near-surface mean wind direction is leftward of the geostrophic forcing. In the case with waves propagating in the $\alpha = +90^\circ$ direction, the near-surface winds experience a wave-following regime, while the opposite is true for the case with $\alpha = -90^\circ$. For the conditions simulated, the scalar wind speed $|\langle \mathbf{u}_a \rangle|$ reveals a 15% wind speed reduction in meters per second at $\zeta/z_i = 0.3$ (~ 100 m) for the 180° case (A5) compared to the 0° case (A1).

5) MOMENTUM FLUX PROFILES

The air–sea interaction community frequently presumes that 10 m is sufficiently high above the water surface to be above the direct influence of the waves (but still within the inertial sublayer where the turbulent momentum flux would be constant with height) such that turbulent fluxes or wind stress measured at this height is thought to represent the total surface stress

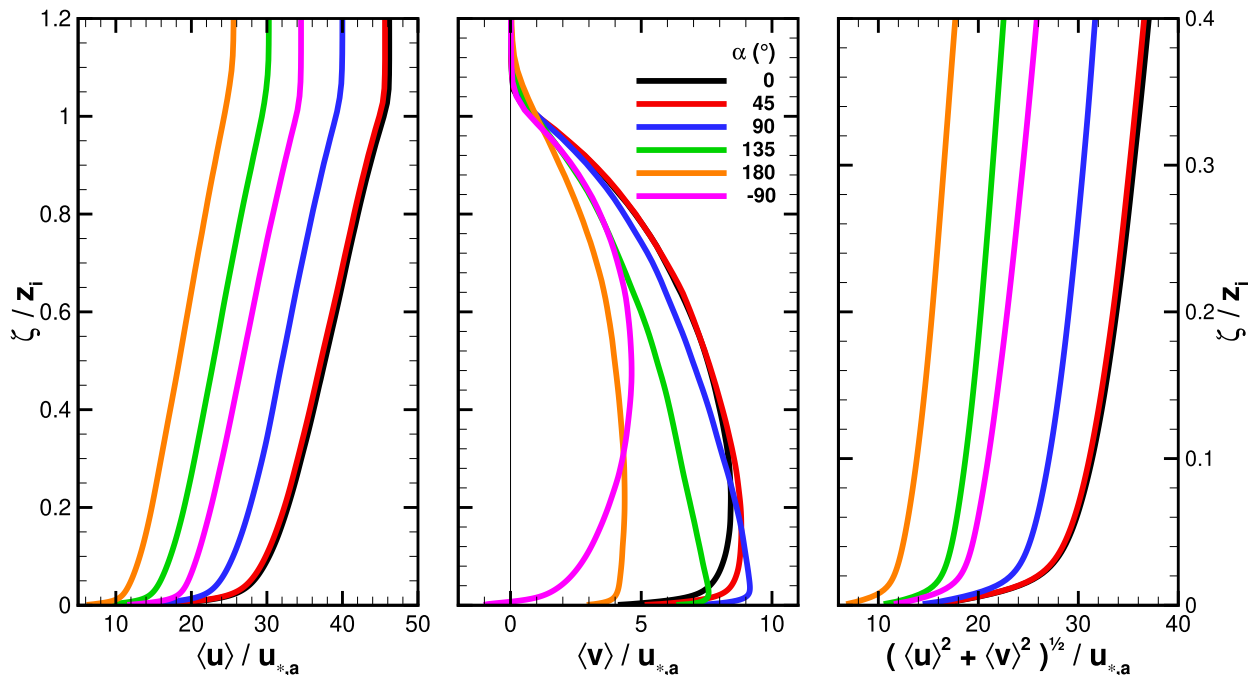


FIG. 7. Vertical profiles of horizontally and time-averaged wind aligned with the (left) positive x direction ($\langle u \rangle$) and (center) the positive y direction ($\langle v \rangle$), and (right) scalar wind speed in response to wave-propagation angle α variations at heights ζ relative to the ABL depth z_i . All quantities have been normalized by $u_{*,a}$. Note that the left two panels show results up to $\zeta/z_i = 1.2$, while the right-hand panel focuses in closer to the surface.

(Toba et al. 2001). Somewhat surprisingly, Sullivan et al. (2014) showed this assumption to be reasonably true even for wind following waves with slight heating and large surface waves when the profiles are computed in wave following coordinates. We now interrogate the influence of wave-propagation angle on that result.

Evaluating Eq. (2) at all heights (i.e., not just at ζ_a) shows how contributions from the various stress components vary with wave-propagation direction (Fig. 8). For each case, the stress components in Fig. 8 have been rotated into the $|\langle \mathbf{u}_a \rangle|$ direction; where (x', y') represent the directions aligned with $(\langle u_a \rangle, \langle v_a \rangle)$. For simplicity, we will at times use the notation U_a to represent $|\langle \mathbf{u}_a \rangle|$.

The first point to note in Fig. 8 is that the total stress in the x' direction does not reflect the total turbulent stress, suggesting that τ_T and $\langle \mathbf{u}_a \rangle$ are not aligned. Variations in the angle between $\langle \mathbf{u}_a \rangle$ and τ_T will be discussed more thoroughly in the next section. A second broad point to note in Fig. 8 is the nonzero pressure stress τ_p to heights well above ζ_a in both the x' and y' directions (right-hand panels).

In the direction aligned with $\langle \mathbf{u}_a \rangle$ (i.e., in the x' direction), pressure-wave slope correlations (τ_p) increase with increasing wave-propagation angle α (Fig. 8). At $\alpha \sim 0^\circ$, τ_p is about 10% of the total in the U_a direction near the surface, while there is also evidence of slight positive pressure drag (wave-driving force on the

atmosphere) at heights above ζ_a . This positive pressure drag disappears by $\alpha = 90^\circ$, and by $\alpha = 180^\circ$ pressure drag is always negative and accounts for approximately 65% of the total stress. The wind stress τ_i diminishes in response to the increasing pressure stress contributions to maintain a nearly constant total stress τ_T profile with height.

In the direction perpendicular to U_a (i.e., in the y' direction), pressure-wave slope correlations reach amplitudes of approximately 0.5 to 0.6 $u_{*,a}^2$ with varying sign. Cases where the wave-propagation direction is nearly perpendicular to $\langle \mathbf{u}_a \rangle$ (i.e., $\alpha = 90^\circ \rightarrow 135^\circ$) and in a direction nearly aligned with the Coriolis force reveal the largest positive pressure drag driving winds in the v_a direction, and in cases where the wave-propagation direction is nearly opposite to the Coriolis force (i.e., $\alpha = -90^\circ$) acts to retard winds in the v_a direction. Near the surface the wind stress τ_i in the y' direction is nearly zero, but quickly increases with height as the atmosphere responds to the wave-induced pressure drag acting to accelerate the flow from beneath. Again, the wind and pressure stress components combine to create a total stress profile that is nearly constant with height below ζ_a .

Above the water surface, it is important to emphasize that the magnitude of the pressure-wave slope correlation depends on the fluctuating pressure amplitude but also how rapidly the computation gridlines (ξ, η)

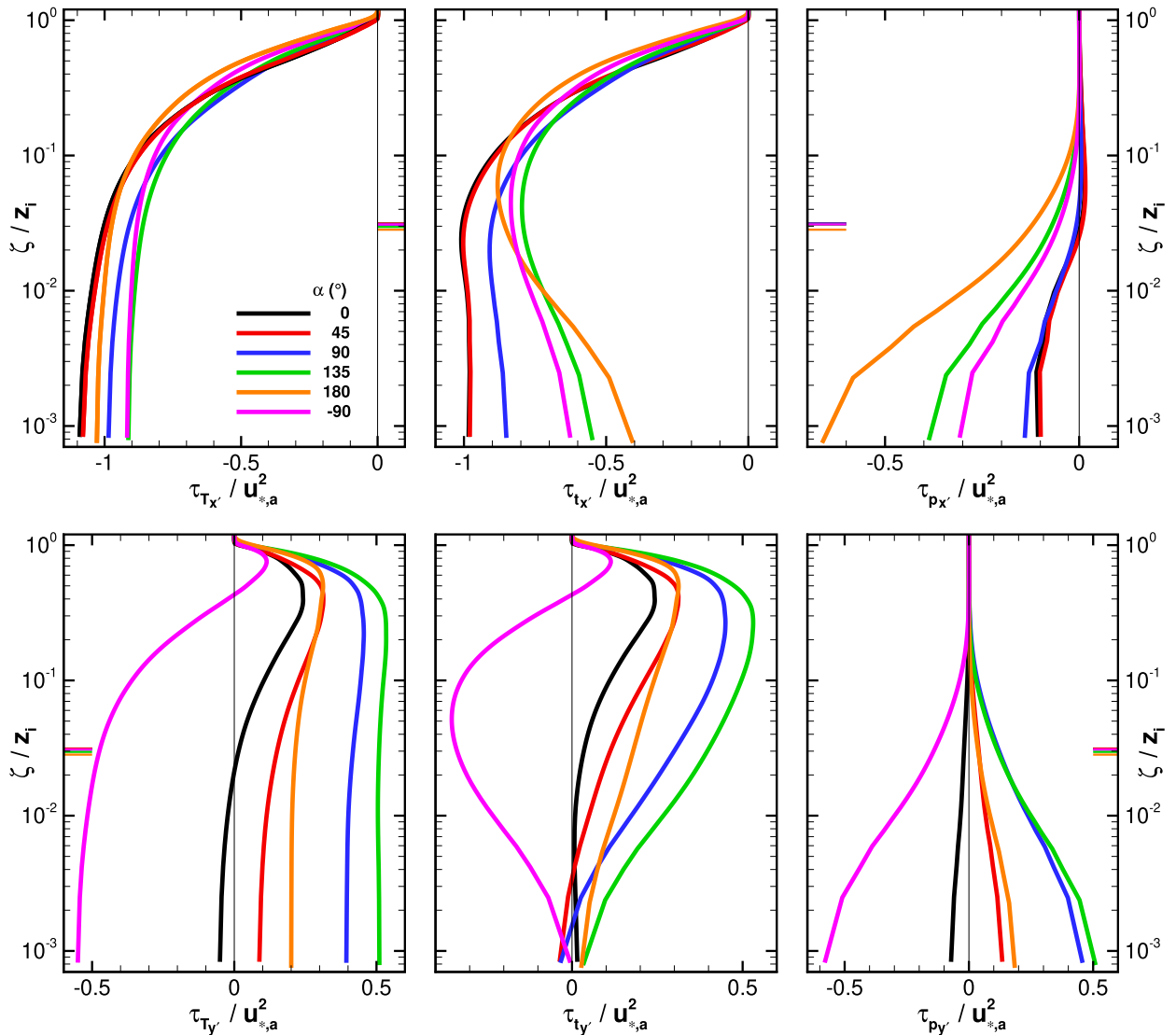


FIG. 8. Vertical profiles of horizontally and time-averaged (left) total stress τ_T , (center) turbulent momentum stress component τ_t , and (right) pressure stress τ_p normalized by u_{*a}^2 for cases A1–A6 in Table 1 with $H_s = 6.4$ m and $\mathbf{U}_g = [10, 0]$ m s $^{-1}$. The stresses have been rotated into an (x', y') coordinate system aligned with $\langle \mathbf{u}_a \rangle = [\langle u_a \rangle, \langle v_a \rangle]$; (top) results aligned with x' , and (bottom) results aligned with y' . The thin black vertical lines mark zero stress, and the short colored lines depict the height $\zeta_a = 10$ m for each case. Note that the abscissa changes scale between panels, and that because of the coordinate rotation, τ_{p_x} and τ_{p_y} at the surface necessarily differ from τ_{p_x} and τ_{p_y} reported in Table 1.

become level surfaces in physical space, that is, how fast the slopes $(\partial\zeta/\partial x, \partial\zeta/\partial y) \rightarrow 0$ as z increases. There are also wave-induced stresses buried in the turbulent stresses (see the middle panels of Figs. 8, 10, and 11), which vary with the slopes of the computational gridlines; no attempt is made to estimate these wave-induced stresses because of the complexity of the underlying surface wave field. Hara and Sullivan (2015) show that for a monochromatic wave the combined sum of pressure and wave induced stresses is however relatively invariant to the coordinate transformation used to map physical space to computational space. As a consequence the total stress in our

computations, (i.e., the sum of the pressure and turbulent stresses) near the water surface exhibits a relatively constant flux region when evaluated in wave following coordinates as shown in the left panels of Figs. 8, 10, and 11.

b. Influence of wave age

1) DEFINITION OF WAVE AGE

The debate concerning the definition of wave age remains unsettled. For example, Högström et al. (2011) argues for C_p/U_a while Hanley et al. (2010, 2011) offers

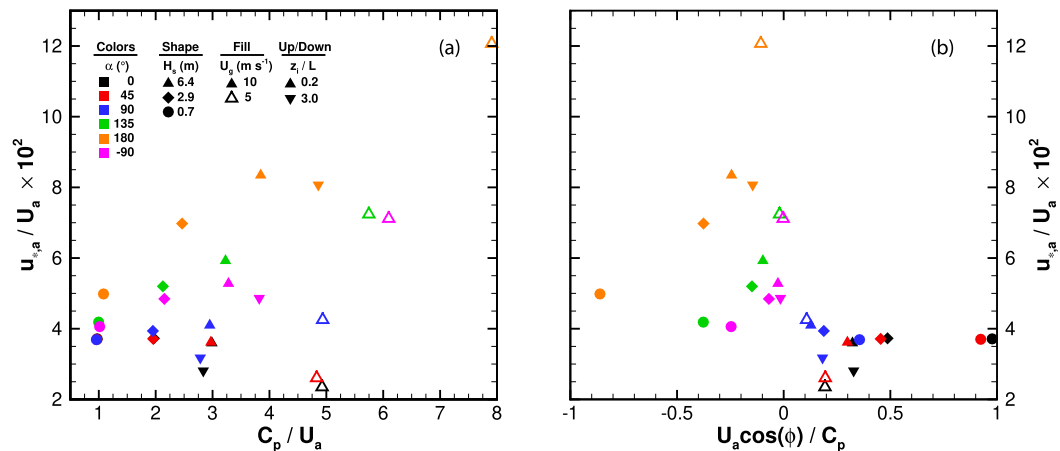


FIG. 9. Variation of $u_{*,a}$ normalized by U_a vs: (a) C_p/U_a , and (b) $U_a \cos(\phi)/C_p$. All values of $u_{*,a}/U_a$ have been multiplied by 100. Results from all simulations are included; colors reflect variations with α , different symbols reflect significant wave height H_s variations, filled vs open symbols reflect variations in \mathbf{U}_g , and upward vs downward pointing triangles depict variations with atmospheric stability z_i/L .

arguments for using inverse wave age corrected for wind–wave misalignment $U_a \cos(\phi)/C_p$. We do not advocate for either definition. Instead, we simply interrogate our numerically generated data and report our findings. As a first step, Fig. 9 presents the variation of $u_{*,a}$ normalized by U_a with both C_p/U_a and $U_a \cos(\phi)/C_p$. Clearly neither definition of wave age (or inverse wave age) collapses the data. The standard definition C_p/U_a , of course, only works for small angles as noted by Höglström et al. (2011). Section 5 proposes an empirical correction for friction velocity that accounts for wave age and wave propagation direction based on the LES results.

2) MOMENTUM FLUX PROFILES

Here, we investigate the combined influence of wave age w_{age} and wave propagation angle on vertical profiles of momentum stress. Using a definition of $w_{\text{age}} = C_p/U_a$, w_{age} in these simulations varies from 0.96 up to 7.91 (where $w_{\text{age}} = 1.2$ is generally classified as wind–wave equilibrium).

(i) Near wind–wave equilibrium

Near wind–wave equilibrium ($0.96 < w_{\text{age}} < 1.08$), pressure–wave slope correlations in both directions reveal a broadly similar response pattern to variations in wave-propagation direction as shown in Fig. 8 (where $2.95 < w_{\text{age}} < 3.85$). However near wind–wave equilibrium (cases C1–C6), τ_p becomes negligible at heights close to ζ_a as the $H_s = 0.7$ m waves travel substantially slower ($C_p = 6 \text{ m s}^{-1}$) compared to the $H_s = 6.4$ m waves in Fig. 8 ($C_p = 18 \text{ m s}^{-1}$) and hence the amplitude of the pressure stress drops as well. The reduction of τ_p with decreasing w_{age} alters the partitioning of the stress components,

but does not drastically modify the overall momentum sink at the water surface. In these cases, the total stress at ζ_a is more closely aligned with the U_a , but when the waves propagate at angles substantially different from U_a , the misaligned component of the total stress τ_{T_y} reaches magnitudes ranging between -0.2 and $+0.4$ of the total stress.

(ii) Increased wave age

Smedman et al. (1999, among others) showed that depending upon the propagation speed of the waves relative to the wind speed (i.e., with increasing w_{age}), that the signature of the surface waves could be felt up to ~ 200 m above the surface implying that observations taken at the 10-m reference height might be impacted by the underlying surface. Similar to Figs. 8 and 10, Fig. 11 presents vertical profiles of the components contributing to the total surface- and time-averaged momentum stress τ_T in a coordinate system aligned with U_a , however Fig. 11 presents results from the simulations with $\mathbf{U}_g = (5, 0) \text{ m s}^{-1}$, that is, cases D1–D6 in Table 1. Wave age for these simulations ranges between $4.83 < w_{\text{age}} < 7.91$.

Under low wind conditions with fast moving waves (i.e., large w_{age}), τ_p in the direction aligned with U_a is both negative (for opposing waves) and positive (for wind-following waves) and of substantially larger magnitude than for the cases with lower w_{age} . Even though τ_p aligned with U_a is of mixed sign, the wind stress τ_{i_x} remains negative for all cases. For waves propagating in directions perpendicular to U_a , τ_{p_x} and τ_{i_y} are nearly constant with height, but they show substantial variation with height for cases where the waves follow or oppose the wind. Inspection of the total stress profiles

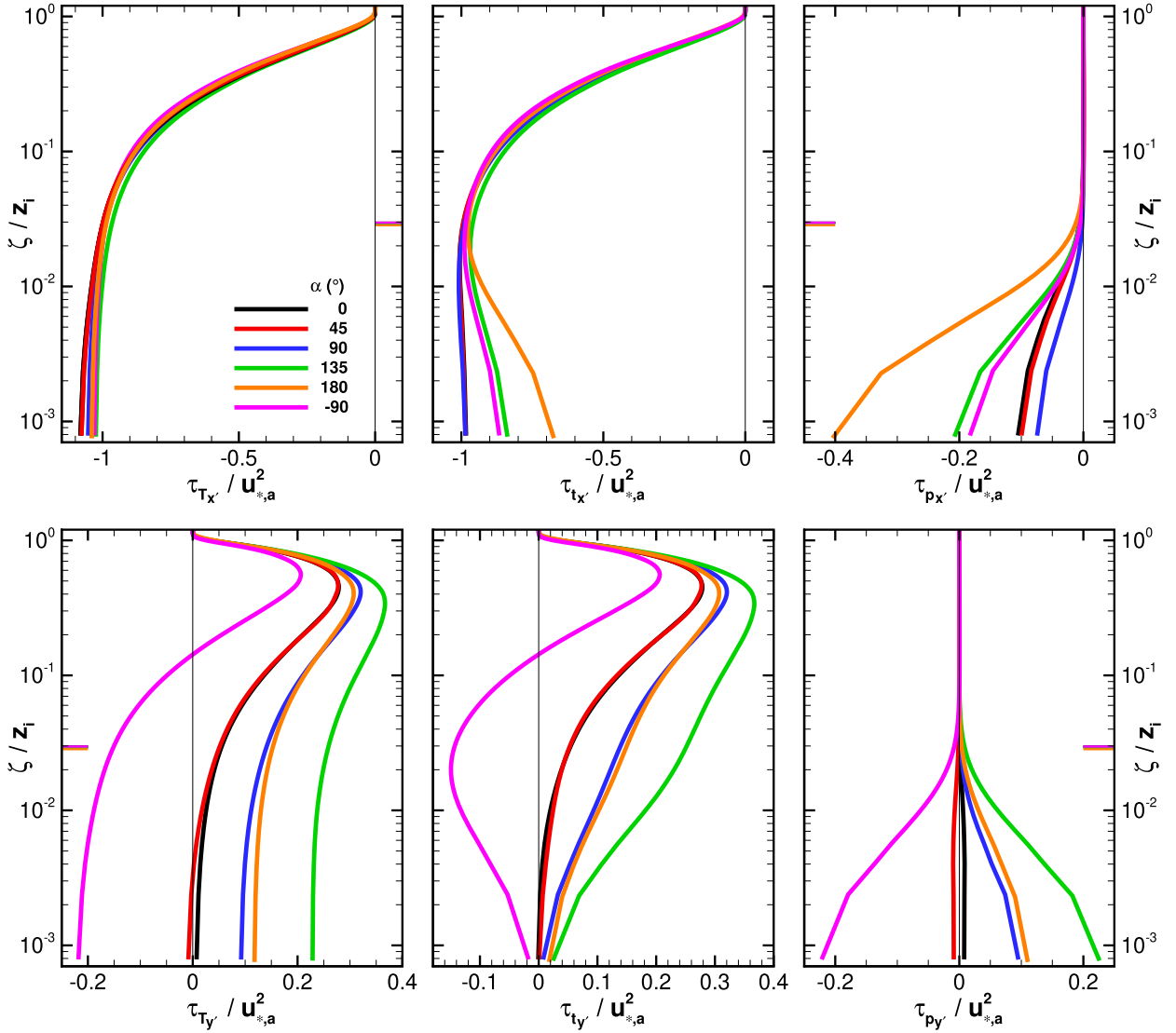


FIG. 10. Vertical profiles of horizontally and time-averaged (left) total stress τ_T , (center) turbulent momentum stress component τ_t , and (right) pressure stress τ_p normalized by u_{*a}^2 for cases C1–C6 in Table 1 with $H_s = 0.7$ m and $\mathbf{U}_g = [10, 0]$ m s $^{-1}$. The stresses have been rotated into an (x', y') coordinate system aligned with $\langle \mathbf{u}_a \rangle = [\langle u_a \rangle, \langle v_a \rangle]$; (top) results aligned with x' , and (bottom) results aligned with y' . The thin black vertical lines mark zero stress, and the short colored lines depict the height $\zeta_a = 10$ m for each case. Note that the abscissa changes scale between panels, and that because of the coordinate rotation, $\tau_{p_x'}$ and $\tau_{p_y'}$ at the surface necessarily differ from τ_{p_x} and τ_{p_y} , reported in Table 1.

for these cases (left-most panels of Fig. 11) clearly demonstrates that increased wave age increases the misalignment between the wind and stress vectors at ζ_a , as pressure drag produced by waves moving in directions different from the overlying wind field drives horizontal motions.

c. Wind and stress vector alignment

For winds and monochromatic waves of a single H_s propagating in directions aligned (and misaligned) with the geostrophic forcing, Sullivan et al. (2008) demonstrated that wave-induced pressure stress alters

the momentum balance compared to flow over flat surfaces; where, increasing wave age changes the overall surface drag and thus the near-surface turning of the wind with respect to the geostrophic forcing Ω . Inspection of Table 1 reveals that Ω not only varies with α , but also with variations in H_s . The momentum balance requires the imposed geostrophic pressure gradient, the Coriolis force, and the total surface drag to balance. Since \mathbf{U}_g and the Coriolis parameter ($f = 1 \times 10^{-4}$ s $^{-1}$) are fixed across all simulations, Ω variations with H_s are largely controlled by the magnitude variation in the surface drag. Note that for the case with $\alpha = 0^\circ$ where

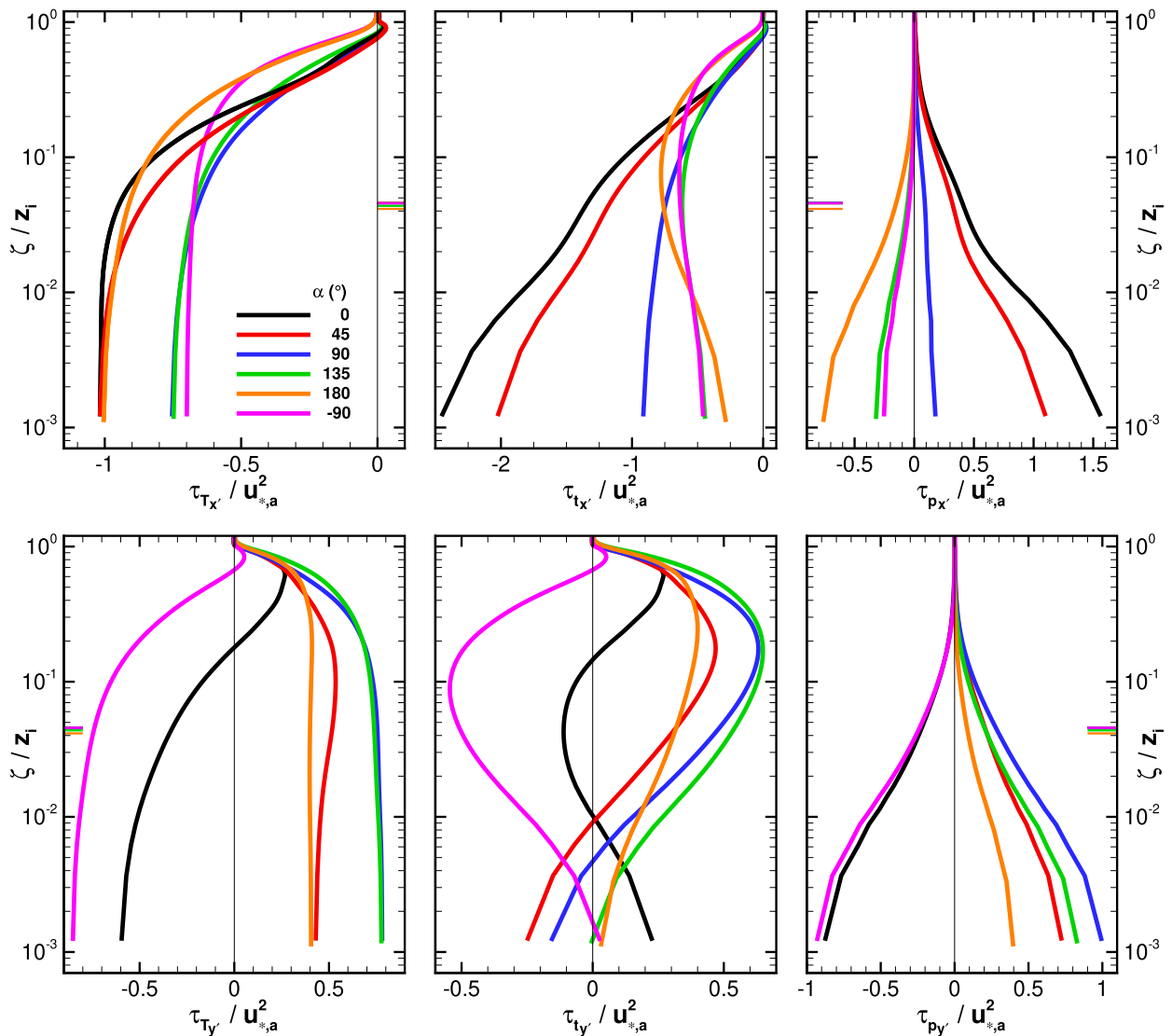


FIG. 11. Vertical profiles of horizontally and time-averaged (left) total stress τ_T , (center) turbulent momentum stress component τ_t , and (right) pressure stress τ_p normalized by u_{*a}^2 for the fourth set of six cases in Table 1 with $H_s = 6.4$ m and $\mathbf{U}_g = [5, 0]$ m s $^{-1}$. The stresses have been rotated into an (x', y') coordinate system aligned with $\langle \mathbf{u}_a \rangle = [\langle u_a \rangle, \langle v_a \rangle]$; (top) results aligned with x' , and the (bottom) results aligned with y' . The thin black vertical lines mark zero stress, and the short colored lines depict the height $\zeta_a = 10$ m for each case. Note that the abscissa changes scale between panels, and that because of the coordinate rotation, τ_{p_x} and τ_{p_y} at the surface necessarily differ from τ_{p_x} and τ_{p_y} reported in Table 1.

the waves are propagating in a direction nearly aligned with the wind, waves with a large significant wave height ($H_s = 6.4$ m) induce reduced drag compared to smaller, slower moving (lower C_p) waves. Cases with $w_{age} > 1.2$ (i.e., cases where the winds and waves are in disequilibrium) reveal increasing wave-induced pressure drag with increasing α and/or Ω . The form drag peaks when $\alpha = 180^\circ$, with the total pressure drag $|\tau_p|_a$ evaluated at ζ_a contributing (13.6%, 9.4%, 1.4%) the momentum stress when $H_s = (6.4, 2.9, 0.7)$, respectively.

When parameterizing surface momentum fluxes, the community frequently assumes opposite alignment

between the 10-m wind vector $\langle \mathbf{u}_a \rangle$ and the surface stress vector $\boldsymbol{\tau}_T = (\tau_{T_x}, \tau_{T_y})$ (see, e.g., Fairall et al. 2003). Using notation:

$$\omega_T = \cos^{-1} \left(\frac{\langle \mathbf{u}_a \rangle \cdot \boldsymbol{\tau}_T}{|\langle \mathbf{u}_a \rangle| |\langle \boldsymbol{\tau}_T \rangle|} \right), \quad (4)$$

to describe the angle between the two vectors, Fig. 12a demonstrates that variations in the wave-propagation direction α produce ω_T variations; where $\omega_T = \pi$ indicates that the stress vector points perfectly in the opposite direction of the wind vector.

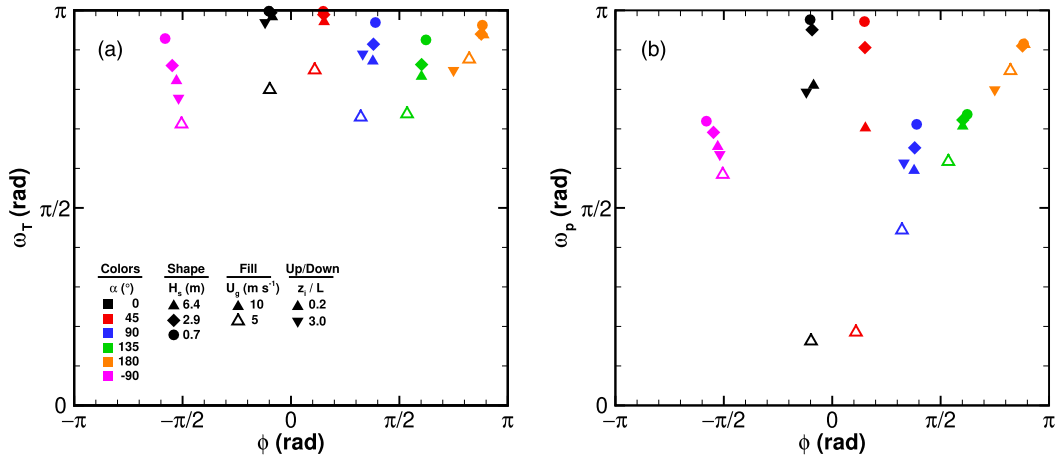


FIG. 12. (a) Variation of the angle ω_T between the 10 m wind vector $\langle \mathbf{u}_a \rangle = (U_a, 0)$ and the total surface stress vector $\boldsymbol{\tau}_T = (\tau_{Tx}, \tau_{Ty})$ and (b) the angle ω_p between $\langle \mathbf{u}_a \rangle$ and the surface pressure stress vector $\boldsymbol{\tau}_p = (\tau_{px}, \tau_{py})$ against the angle ϕ between $\langle \mathbf{u}_a \rangle$ and the wave-propagation direction. All quantities are presented in radians. Results from all simulations are included; colors reflect variations with α , different symbols reflect significant wave height H_s variations, filled vs open symbols reflect variations in \mathbf{U}_g , and upward vs downward pointing triangles depict variations with atmospheric stability z_i/L .

In general, increased w_{age} results in larger misalignment between $\langle \mathbf{u}_a \rangle$ and $\boldsymbol{\tau}_T$ (ω_T reduces to values smaller than π with increasing w_{age}). Increased w_{age} also shifts the 10-m wind direction more toward that of geostrophic forcing (i.e., $\phi \rightarrow 0$ with increasing w_{age}). Waves propagating in directions perpendicular to the 10-m wind direction ($\phi = \pm\pi/2$) most dramatically alter ω_T . Geernaert et al. (1993), Rieder et al. (1994), and Grachev et al. (2003) all found similar results in their field observations and inferred causality but were unable to isolate wind versus pressure stress contributions.

Therefore to explain these ω_T results further, Fig. 12b interrogates the angle between $\langle \mathbf{u}_a \rangle$ and the pressure stress vector $\boldsymbol{\tau}_p = (\tau_{px}, \tau_{py})$ at the surface, that is, ω_p :

$$\omega_p = \cos^{-1} \left(\frac{\langle \mathbf{u}_a \rangle \cdot \boldsymbol{\tau}_p}{|\langle \mathbf{u}_a \rangle| |\boldsymbol{\tau}_p|} \right), \quad (5)$$

which represents the wave-induced contribution to $\boldsymbol{\tau}_T$ [see Eq. (2)]. Parameters w_{age} and α both have an $O(1)$ influence on the alignment between $\langle \mathbf{u}_a \rangle$ and $\boldsymbol{\tau}_p$. Wave age w_{age} influences ω_p most when the winds and waves propagate generally in the same direction (i.e., $\phi \sim 0$ rad); where for large w_{age} , surface pressure stress is nearly aligned with the 10-m wind.

5. Parameterization

Many parameterizations have been proposed for describing wave influences surface drag (e.g., Charnock 1955; Taylor and Yelland 2001; Drennan et al. 2003; Fairall et al. 2003; Drennan et al. 2005; Davis et al. 2008;

Andreas et al. 2012; Edson et al. 2013; Höglström et al. 2018). In this section we use our LES results to test two of those parameterizations in an attempt to understand the impact wind–wave alignment has on those parameterizations and to make an attempt to account for wind–wave alignment’s influence within one of them.

a. Nondimensional surface roughness

Previous research (e.g., Drennan et al. 1999, 2003, 2005)² has suggested the following variation of z_o normalized by the significant wave height H_s and inverse wave age (where they define inverse wave age as: $w_{\text{age}}^{-1} = u_* / C_p$):

$$\frac{z_o}{H_s} = 3.35 \left(\frac{u_*}{C_p} \right)^{3.4}. \quad (6)$$

Observations from a number of offshore experiments agree with their formulation for young waves (right side of Fig. 13a). For swell, or old waves (left side of Fig. 13a), the data exhibits significant scatter and the bin-averaged mean z_o/H_s deviates positively from what Eq. (6) would predict.

In an attempt to elucidate the mechanisms responsible for the observed scatter in z_o/H_s when waves are old (swell), we now test Drennan et al.’s parameterization using our neutrally stratified LES results. Here, the

²Note that Drennan et al. (2005) use the notation c_p to represent the phase speed of the peak in the wave spectrum, while here in this paper C_p is used.

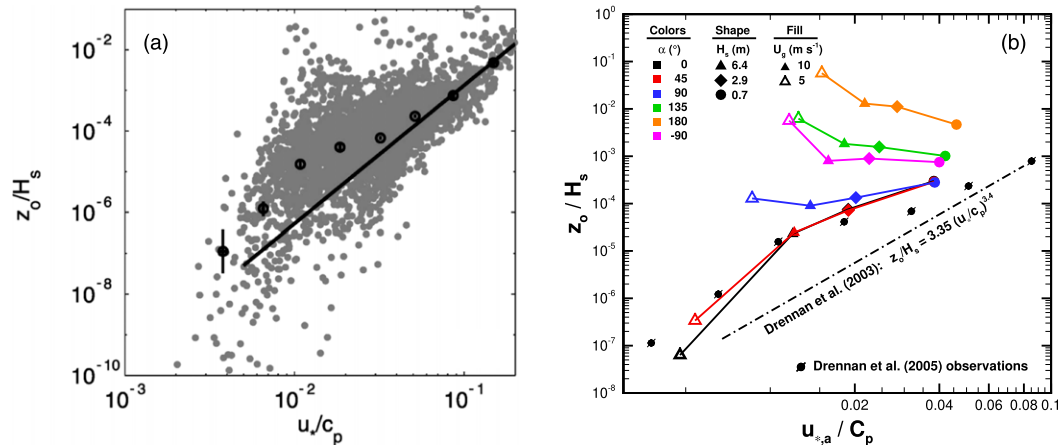


FIG. 13. (a) Nondimensional surface roughness z_o/H_s as a function of inverse wave age, $w_{\text{age}}^{-1} = u_*/c_p$ from seven different offshore field campaigns (from Drennan et al. 2005), where u_* is the observed momentum stress at 10 m, H_s is significant wave height, and c_p represents the phase speed of the peak in the wave spectrum. The black open circles are bin-averaged means, and the error bars represent two standard errors about the mean. The solid black line depicts the Drennan et al. (2003) curve [Eq. (6)]. (b) LES-derived nondimensional surface roughness z_o/H_s , as a function of $w_{\text{age}}^{-1} = u_{*,a}/C_p$. The conditionally neutral LES results are colored by α (the angle between the wave propagation direction and the geostrophic forcing direction). Each of these angles is presented for three different significant wave heights H_s and for a geostrophic wind of 10 m s^{-1} . For the largest/fastest waves ($H_s = 6.4 \text{ m}$, $C_p = 18 \text{ m s}^{-1}$), the open symbols represent LES results for a geostrophic wind of 5 m s^{-1} . The colored lines connect LES results for similar α , the black filled circles with slashes mark Drennan et al.'s (2005) bin-averaged observations, and the black dash-dot line presents Drennan et al.'s (2003) parameterization.

LES-derived bulk z_o of the surface is calculated based upon an assumed logarithmic wind profile with height using the 10 m U_a and $u_{*,a}$, via:

$$z_o = 10 \exp\left(\frac{U_a \kappa}{u_{*,a}}\right), \quad (7)$$

where κ is the von Kármán constant with a value of 0.4. The LES results compare surprisingly well with Drennan et al.'s (2003, 2005) data [compare Figs. 13a and 13b, using the bin-averaged Drennan et al. (2005) data as a reference]. Importantly, the LES results suggest that the variability of z_o/H_s at large w_{age} discussed by Drennan et al. (2005) can largely be explained by incorporating the propagation direction of the waves (i.e., reduced z_o when swell propagates with the waves and incrementally increasing z_o as the waves transition to propagate at directions counter to the driving pressure gradient, peaking at 180° , and reducing again at -90°). The relatively large z_o values for the lower wind speed cases (open triangles) with waves propagating at directions different to U_g should be taken with caution since outdoors the small waves that carry much of the drag (Sullivan et al. 2014) would dissipate semirapidly—a feature which we cannot reproduce here because our waves are imposed and are therefore unable to respond to the overlying wind field.

b. Direct relationship between U_a and $u_{*,a}$

In an attempt to account for wave state in parameterizing drag wind relationships, Andreas et al. (2012) abandoned traditional velocity-squared drag law formulations and found that the following direct relationship between the 10-m wind U_a and the drag of underlying wavy surfaces (characterized by $u_{*,a}$ observed at 10 m):

$$u_{*,A} = 0.239 + 0.0433 \left\{ (U_a - 8.271) + [0.120 (U_a - 8.271)^2 + 0.181]^{1/2} \right\} \quad (8)$$

reproduces data from 10 different offshore field campaigns for winds up to about 20 m s^{-1} . Here, we use the subscript A to reflect a friction velocity prediction using Andreas et al.'s (2012) formulation presented in Eq. (8).

Andreas et al.'s (2012) relationship [Eq. (8)] works reasonably well for the LES data when the waves are nearly aligned with the mean pressure gradient (red and black symbols, Fig. 14a); although we do not have access to wave-state information for the Coupled Boundary Layers Air–Sea Transfer–Low Wind (CBLAST-Low) experiment (Edson et al. 2007; Mahrt et al. 2016), the trends in the CBLAST-Low data reflect a similar character to that found in the LES. However, Eq. (8)

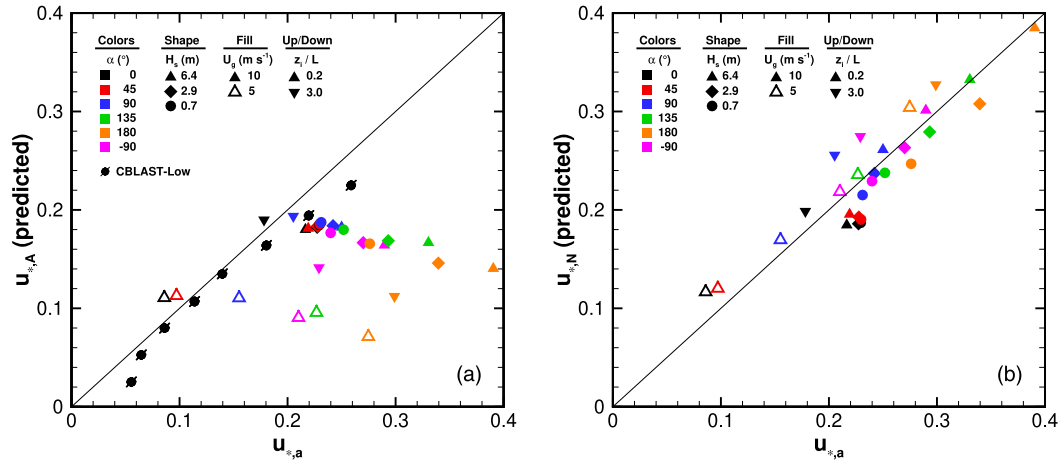


FIG. 14. (a) Predictions of the friction velocity $u_{*,A}$ based upon Eq. (8) using U_a from each of the LES runs compared to $u_{*,a}$ predicted directly by the LES and to observations from CBLAST-Low (Edson et al. 2007; Mahrt et al. 2016) under neutral conditions (black filled circles with slashes). (b) Predictions of $u_{*,N}$ based upon Eq. (9) compared to the same $u_{*,a}$ from the LES. In both panels, the symbol colors, shapes, and fills are the same as those discussed in Fig. 13, however this figure also includes the stable cases with $U_g = 10 \text{ m s}^{-1}$ and $H_s = 6.4 \text{ m}$ as downward triangles.

dramatically under predicts the friction velocity compared to the LES when the waves propagate at large angles relative to the wind direction (Fig. 14a); a finding which Andreas et al. (2012) were only able to hint at with their observations.

Using the LES data, we can empirically correct $u_{*,A}$ to account for the influence of swell:

$$u_{*,N} = u_{*,A} \{1 + \gamma w_{\text{age}} [1 - \cos(\phi)]\}, \quad (9)$$

where, the subscript N denotes our new formulation, $w_{\text{age}} = C_p/u_{*,A}$, ϕ is the angle between U_a and the propagation direction of the surface waves (see Table 1 for actual values), and $\gamma = 0.007$ is a small dimensionless parameter. Estimating the friction velocity $u_{*,N}$ via Eq. (9) substantially collapses the predictions along the one-to-one line compared with $u_{*,a}$ from the LES (Fig. 14b); even the stable cases fit this formulation (downward pointing triangles).

Note that Eq. (9) represents a simple prescription for surface drag based on wind speed but includes essentially linear corrections for wave age and wind-wave direction. Thus, Eq. (9) is a bulk formula in a similar spirit to the highly developed COARE formula proposed by Fairall et al. (2003, 2011). Notice also that application of Eq. (9) requires wave information and cannot be blindly used by an atmospheric model that is unaware of the surface wave state. One would either need wave-state observations (e.g., section 6) or a more advanced large-scale numerical weather prediction model such as those developed at ECMWF that are coupled to a spectral

wave model (Janssen 2004) allowing for full interaction between winds and waves based on the quasi-linear theory of wind-wave generation proposed by Janssen (1989, 1991).

6. Testing in a regional climate model: WRF

WRF's MYNN model provides a number of formulations that attempt to account for the influence of surface waves (e.g., Charnock 1955; Taylor and Yelland 2001; Fairall et al. 2003; Davis et al. 2008) on surface drag. To test the formulation presented in Eq. (9), WRF's MYNN model was first modified to include an option to use Andreas et al.'s (2012) formulation. We were then able to incorporate the modification presented in Eq. (9). Once these new formulations were introduced into the MYNN model, we tested 3D WRF predictions using Eq. (9) as the surface layer parameterization in MYNN against the FINO1 tower observations.

To incorporate FINO1 wave-state information, we modified WRF to read wave-state variables derived from the FINO1 observations; these variables include 1) significant wave height, 2) significant wave period, and 3) wave propagation direction. To connect the observations with Eq. (9), we 1) assume that 30 m is sufficiently deep to satisfy deep water linear wave theory and construct a phase velocity $C_p = (gT)/(2\pi)$, and 2) define the angle between the near-surface wind direction and wave propagation direction ϕ using the wind direction in WRF's lowest model level and the observed wave propagation direction. When integrated into the WRF

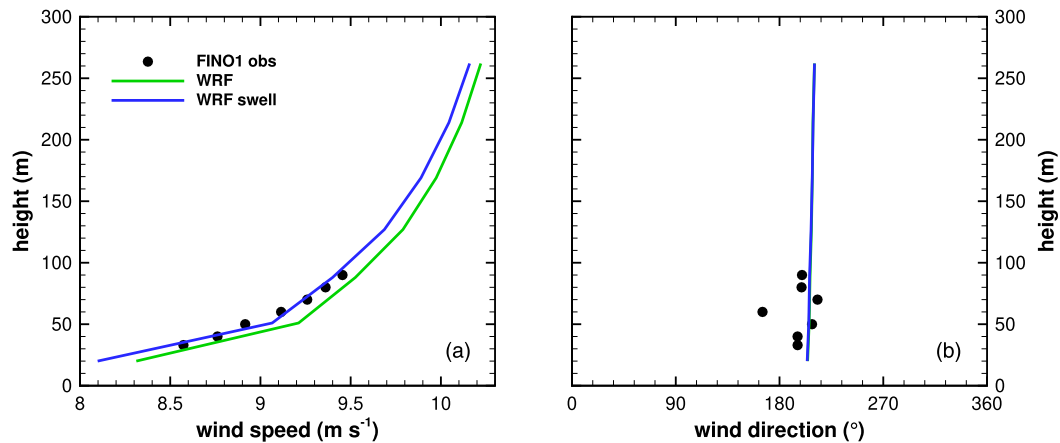


FIG. 15. Vertical profiles of annually averaged: (a) wind speed and (b) wind direction at the FINO1 tower for 2006. Black circles depict the FINO1 tower observations, the green line depicts results from a 3D WRF simulation using WRF's traditional Charnock (1955) formulation for z_0 , and the blue line depicts results from a 3D WRF simulation where the surface friction velocity is determined using Eq. (9) using the observed hourly wave data at FINO1.

simulations, the wave-state observations are averaged over one minute and held constant during the subsequent minute of the simulation.

We used a three-dimensional, limited area version of WRF V3.6.1 to simulate an entire year (2006) over the North Sea. The numerical simulations were configured following standard wind resource assessment practices. Each simulation was carried daily for 30 h starting at 0000 UTC. The first 6 h were used as a spinup period. The output was saved every 20 min for 24 h between 0600 UTC on the first day and 0600 UTC on the second day. The computational domain covered the North Sea and northeastern Europe centered on the FINO1 tower and was discretized using nested computational domains with grid cell sizes of 9, 3, and 1 km. The innermost domain covered an area of $100 \text{ km} \times 100 \text{ km}$. In the vertical direction we used a stretched grid with 37 levels. Initial and boundary conditions were derived from National Centers for Environmental Prediction (NCEP)'s Final Operational Global Analysis (Schuster 2000). Geostrophic forcing and advection tendencies were extracted from the NCEP analysis data as well as initial profiles of the wind velocity components, potential temperature, and humidity.

To assess the influence of the new parameterization [Eq. (9)], we carried out two simulations. A baseline simulation used the Charnock (1955) parameterization on all domains, while the second simulation includes the new surface layer parameterization on the innermost domain only and used the Charnock (1955) parameterization on the outer domains. This strategy assumes that the wave state in the broad area

surrounding the FINO1 tower can be represented by the measurements at the tower. In the simulation including the new parameterization including wave-propagation direction influences, FINO1-observed wave-state information was updated hourly and held constant for the subsequent simulated hour (i.e., no attempt was made to interpolate between the hourly observations).

Results of the two three-dimensional WRF simulations are shown in Fig. 15. Annually averaged wind speed measurements at the FINO1 tower are presented with black symbols, the green line denotes simulation results using the Charnock (1955) parameterization on all domains, and the blue line denotes three-dimensional WRF results with the new parameterization accounting for the effects of nonequilibrium waves on the innermost domain. Although the differences between two WRF simulations are relatively small (Fig. 15a), better agreement between the observations and the simulation accounting for the effect of swell is apparent. During 2006 at FINO1, winds and waves were generally misaligned (see Fig. 1). Therefore, when incorporating wave influences into the simulations, the increased drag induced by swell propagating at directions counter to the winds should act to increase the surface drag and reduce wind speeds; Fig. 15a reveals that the wave-state parameterization has precisely this influence on the annually averaged wind profile predictions. The simulated wind direction in both WRF simulations direction is also in generally good agreement with the data (Fig. 15b). Using the new surface layer parameterization mean absolute error (MAE) in hub height winds (at 91 m) reduces from 2.81 to

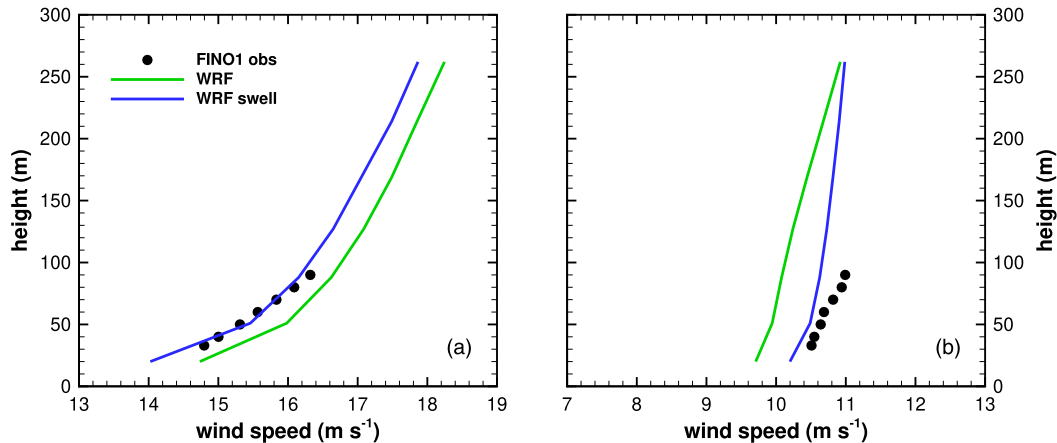


FIG. 16. Comparison of simulations and observations of the wind speed at FINO1 on (a) 9 Oct 2006 and (b) 13 Nov 2006. Symbols represent observations, and lines are simulation results as in Fig. 15. Here, 9 Oct 2006 reflects a day when swell propagated in a direction opposing the winds, and 13 Nov 2006 reflects a day when winds and waves were nearly aligned.

2.77 m s^{-1} , while the RMSE reduces from 3.60 to 3.54 m s^{-1} . These annually averaged error reductions are relatively modest, but certainly reflect increased predictive skill.

Interrogating specific cases clearly demonstrates the importance of the new parameterization. In Fig. 16, observed and simulated wind speed are shown for two different days, 9 October and 13 November 2006. On 9 October, the angle between the observed wind direction and the wave-propagation direction was 180° (opposite) and the wave height 1.3 m . On 13 November the angle between the observed winds and waves was 60° (nearly aligned) and the wave height was $\sim 3 \text{ m}$. Waves opposing the winds increases the surface drag reducing predicted hub-height wind speeds (Fig. 16a); when waves are aligned with the winds (Fig. 16b), wave-induced surface drag accelerates the wind. In both cases, the simulation accounting for nonequilibrium winds/waves results in significantly better agreement with the observations with wind speed differences at 100 m between the two simulations of about 1 m s^{-1} .

7. Discussion and conclusions

Fast moving swell induces pressure drag at the water surface. The magnitude and direction of the induced pressure drag force varies both with w_{age} and with the directionality of the waves relative to the wind direction. Even under wind-wave equilibrium, waves of varying propagation direction induce pressure drag in the direction perpendicular to the wind direction at $\zeta_a = 10 \text{ m}$. Increased w_{age} amplifies the atmospheric response to the direction that the underlying waves propagate and the

height to which wave-induced pressure forces are felt. Swell propagating in directions different from the overlying wind field alters the angle between wind and stress vectors. Neither the definition of w_{age} argued for by Höglström et al. (2011) nor that for w_{age}^{-1} by Hanley et al. (2010, 2011) collapse the influence of wind-wave misalignment on the friction velocity u_{*a} .

Misaligned winds/waves increase the surface pressure drag by nearly a factor of 2 relative to the turbulent stress for the extreme case where waves propagate at 180° compared to the pressure gradient forcing; increased atmospheric stability increases the wave-induced pressure stress again by $\sim 10\%$. Pressure drag induced by waves propagating in directions different from the 10-m wind vector alters the alignment between the 10-m wind and surface stress vectors. Wind speeds at 100 m reduce by nearly 15% for the 180° case compared to the 0° case; these impacts diminish with decreasing w_{age} .

In a broad sense, these results suggest that one needs information on winds, temperature, and wave state to upscale buoy measurements. Wind-wave alignment likely explains large scatter in nondimensional surface roughness z_o/H_s under swell-dominated conditions (i.e., at low inverse wave age w_{age}^{-1}). Andreas et al.'s (2012) relationship between u_* and the 10-m wind speed under predicts the increased u_* produced by wave-induced pressure drag. Incorporating wave-state (speed and direction) influences in parameterizations improves predictive skill; a result supporting the need to incorporate wave models (e.g., ECMWF 2017; WAVEWATCH III Development Group 2016) into offshore weather forecasting efforts.

Acknowledgments. Authors EGP, PPS, BK, JD, LM acknowledge support from DOE Office of Energy Efficiency and Renewable Energy DE-EE0005373. Vestas Wind Systems A/S provided substantial computational resources in support of this project while the majority of the computations and analysis used resources of the National Energy Research Scientific Computing Center, a DOE Office of Science User Facility supported by the Office of Science of the U.S. Department of Energy under Contract DE-AC02-05CH11231. NCAR is sponsored by the National Science Foundation.

REFERENCES

- Andreas, E. L., L. Mahrt, and D. Vickers, 2012: A new drag relation for aerodynamically rough flow over the ocean. *J. Atmos. Sci.*, **69**, 2520–2537, <https://doi.org/10.1175/JAS-D-11-0312.1>.
- Beare, R. J., and Coauthors, 2006: An intercomparison of large-eddy simulations of the stable boundary layer. *Bound.-Layer Meteor.*, **118**, 247–272, <https://doi.org/10.1007/s10546-004-2820-6>.
- Bundesamt für Seeschifffahrt und Hydrographie, 2016: FINO1. https://www.bsh.de/EN/DATA/Marine_environment_monitoring_network/marine_environment_monitoring_network_node.html.
- Charnock, H., 1955: Wind stress on a water surface. *Quart. J. Roy. Meteor. Soc.*, **81**, 639–640, <https://doi.org/10.1002/qj.49708135027>.
- Csanady, G. T., 2001: *Air-Sea Interaction: Laws and Mechanisms*. Cambridge University Press, 239 pp., <https://doi.org/10.1017/CBO9781139164672>.
- Davis, C., and Coauthors, 2008: Prediction of landfalling hurricanes with the Advanced Hurricane WRF model. *Mon. Wea. Rev.*, **136**, 1990–2005, <https://doi.org/10.1175/2007MWR2085.1>.
- Davis, K. J., N. Gamage, C. R. Hagelberg, C. Kiemle, D. H. Lenschow, and P. P. Sullivan, 2000: An objective method for deriving atmospheric structure from airborne lidar observations. *J. Atmos. Oceanic Technol.*, **17**, 1455–1468, [https://doi.org/10.1175/1520-0426\(2000\)017<1455:AOMFDA>2.0.CO;2](https://doi.org/10.1175/1520-0426(2000)017<1455:AOMFDA>2.0.CO;2).
- Deardorff, J. W., 1972: Three-dimensional numerical modeling of the planetary boundary layer. *Workshop on Micrometeorology*, D. A. Haugen, Ed., Amer. Meteor. Soc., 271–311.
- Donelan, M. A., J. Hamilton, and W. H. Hui, 1985: Directional spectra of wind-generated waves. *Philos. Trans. Roy. Soc. London*, **315A**, 509–562, <https://doi.org/10.1098/rsta.1985.0054>.
- Drennan, W. M., K. K. Kahma, and M. A. Donelan, 1999: On momentum flux and velocity spectra over waves. *Bound.-Layer Meteor.*, **92**, 489–515, <https://doi.org/10.1023/A:1002054820455>.
- , H. C. Graber, D. Hauser, and C. Quentin, 2003: On the wave age dependence of wind stress over pure wind seas. *J. Geophys. Res.*, **108**, 8062, <https://doi.org/10.1029/2000JC000715>.
- , P. K. Taylor, and M. J. Yelland, 2005: Parameterizing the sea surface roughness. *J. Phys. Oceanogr.*, **35**, 835–848, <https://doi.org/10.1175/JPO2704.1>.
- ECMWF, 2017: Part VII: ECMWF Wave Model. IFS Doc. CY43R3, European Center for Medium-Range Weather Forecasts, 99 pp., <https://www.ecmwf.int/sites/default/files/elibrary/2017/17739-part-vii-ecmwf-wave-model.pdf>.
- Edson, J., and Coauthors, 2007: The coupled boundary layers and air-sea transfer experiment in low winds. *Bull. Amer. Meteor. Soc.*, **88**, 341–356, <https://doi.org/10.1175/BAMS-88-3-341>.
- Edson, J. B., and Coauthors, 2013: On the exchange of momentum over the open ocean. *J. Phys. Oceanogr.*, **43**, 1589–1610, <https://doi.org/10.1175/JPO-D-12-0173.1>.
- Fairall, C. W., E. F. Bradley, J. E. Hare, A. A. Grachev, and J. B. Edson, 2003: Bulk parameterization of air-sea fluxes: Updates and verification for the COARE algorithm. *J. Climate*, **16**, 571–591, [https://doi.org/10.1175/1520-0442\(2003\)016<0571:BPOASF>2.0.CO;2](https://doi.org/10.1175/1520-0442(2003)016<0571:BPOASF>2.0.CO;2).
- , and Coauthors, 2011: Implementation of the Coupled Ocean-Atmosphere Response Experiment flux algorithm with CO₂, dimethyl sulfide, and O₃. *J. Geophys. Res.*, **116**, C00F09, <https://doi.org/10.1029/2010JC006884>.
- FuE-Zentrum FH Kiel GmbH, 2013: FINO1: Forschungsplattformen in Nord- und Ostsee Nr. 1. <http://www.fino1.de/en/>.
- Geernaert, G. L., 1988: Measurements of the angle between the wind vector and wind stress vector in the surface layer over the North Sea. *J. Geophys. Res.*, **93**, 8215–8220, <https://doi.org/10.1029/JC093iC07p08215>.
- , F. Hansen, M. Courtney, and T. Herbers, 1993: Directional attributes of the ocean surface wind stress vector. *J. Geophys. Res.*, **98**, 16 571–16 582, <https://doi.org/10.1029/93JC01439>.
- Grachev, A. A., and C. W. Fairall, 2001: Upward momentum transfer in the marine boundary layer. *J. Phys. Oceanogr.*, **31**, 1698–1711, [https://doi.org/10.1175/1520-0485\(2001\)031<1698:UMTITM>2.0.CO;2](https://doi.org/10.1175/1520-0485(2001)031<1698:UMTITM>2.0.CO;2).
- , —, J. E. Hare, J. B. Edson, and S. D. Miller, 2003: Wind stress vector over ocean waves. *J. Phys. Oceanogr.*, **33**, 2408–2429, [https://doi.org/10.1175/1520-0485\(2003\)033<2408:WSVOOW>2.0.CO;2](https://doi.org/10.1175/1520-0485(2003)033<2408:WSVOOW>2.0.CO;2).
- Hanley, K. E., and S. E. Belcher, 2008: Wave-driven wind jets in the marine atmospheric boundary layer. *J. Atmos. Sci.*, **65**, 2646–2660, <https://doi.org/10.1175/2007JAS2562.1>.
- , —, and P. P. Sullivan, 2010: A global climatology of wind-wave interaction. *J. Phys. Oceanogr.*, **40**, 1263–1282, <https://doi.org/10.1175/2010JPO4377.1>.
- , —, and —, 2011: Reply. *J. Phys. Oceanogr.*, **41**, 1814–1817, <https://doi.org/10.1175/JPO-D-11-051.1>.
- Hara, T., and P. P. Sullivan, 2015: Wave boundary layer turbulence over surface waves in a strongly forced condition. *J. Phys. Oceanogr.*, **45**, 868–883, <https://doi.org/10.1175/JPO-D-14-0116.1>.
- Högström, U., A.-S. Smedman, A. Semedo, and A. Rutgersson, 2011: Comments on A global climatology of wind-wave interaction. *J. Phys. Oceanogr.*, **41**, 1811–1813, <https://doi.org/10.1175/JPO-D-10-05015.1>.
- , E. Sahlée, A.-S. Smedman, A. Rutgersson, E. Nilsson, K. K. Kahma, and W. M. Drennan, 2018: The transition from downward to upward air-sea momentum flux in swell-dominated light wind conditions. *J. Atmos. Sci.*, **75**, 2579–2588, <https://doi.org/10.1175/JAS-D-17-0334.1>.
- Janssen, P. A. E. M., 1989: Wave-induced stress and the drag of air flow over sea waves. *J. Phys. Oceanogr.*, **19**, 745–754, [https://doi.org/10.1175/1520-0485\(1989\)019<0745:WISATD>2.0.CO;2](https://doi.org/10.1175/1520-0485(1989)019<0745:WISATD>2.0.CO;2).
- , 1991: Quasi-linear theory of wind-wave generation applied to wave forecasting. *J. Phys. Oceanogr.*, **21**, 1631–1642, [https://doi.org/10.1175/1520-0485\(1991\)021<1631:QLTOWW>2.0.CO;2](https://doi.org/10.1175/1520-0485(1991)021<1631:QLTOWW>2.0.CO;2).
- , 2004: *The Interaction of Ocean Waves and Wind*. Cambridge University Press, 379 pp., <https://doi.org/10.1017/CBO9780511525018>.
- Komen, G. J., L. Cavaleri, M. Donelan, K. Hasselmann, S. Hasselmann, and P. A. E. M. Janssen, 1994: *Dynamics and Modelling of Ocean Waves*. Cambridge University Press, 532 pp.
- Larsén, X. G., V. K. Makin, and A.-S. Smedman, 2003: Impact of waves on the sea drag: Measurements in the Baltic sea and a

- model interpretation. *J. Atmos. Ocean Sci.*, **9**, 97–120, <https://doi.org/10.1080/10236730310001606308>.
- Li, P. Y., D. Xu, and P. A. Taylor, 2000: Numerical modelling of turbulent airflow over water waves. *Bound.-Layer Meteor.*, **95**, 397–425, <https://doi.org/10.1023/A:1002677312259>.
- Mahrt, L., E. L. Andreas, J. B. Edson, D. Vickers, J. Sun, and E. G. Patton, 2016: Coastal zone surface stress with stable stratification. *J. Phys. Oceanogr.*, **46**, 95–105, <https://doi.org/10.1175/JPO-D-15-0116.1>.
- Nakanishi, M., and H. Niino, 2004: An improved Mellor-Yamada level-3 model with condensation physics: Its design and verification. *Bound.-Layer Meteor.*, **112**, 1–31, <https://doi.org/10.1023/B:BOUN.0000020164.04146.98>.
- Phillips, O. M., 1977: *The Dynamics of the Upper Ocean*. Cambridge University Press, 336 pp.
- Rieder, K. F., J. A. Smith, and R. A. Weller, 1994: Observed directional characteristics of the wind, wind stress, and surface-waves on the open-ocean. *J. Geophys. Res.*, **99**, 22 589–22 596, <https://doi.org/10.1029/94JC02215>.
- Rutgersson, A., A. Smedman, and U. Högström, 2001: Use of conventional stability parameters during swell. *J. Geophys. Res.*, **106**, 27 117–27 134, <https://doi.org/10.1029/2000JC000543>.
- Schuster, D., 2000: NCEP FNL Operational Model Global Tropospheric Analyses, continuing from July 1999. Research Data Archive at the National Center for Atmospheric Research, Computational and Information Systems Laboratory, accessed 1 October 2009, <https://doi.org/10.5065/D6M043C6>.
- Semedo, A., K. Sušelj, A. Rutgersson, and A. Sterl, 2011: A global view on the wind sea and swell climate and variability from ERA-40. *J. Climate*, **24**, 1461–1479, <https://doi.org/10.1175/2010JCLI3718.1>.
- Skamarock, W. C., and Coauthors, 2008: A description of the Advanced Research WRF version 3. NCAR Tech. Note NCAR/TN-475+STR, 113 pp., <https://doi.org/10.5065/D68S4MVH>.
- Smedman, A.-S., U. Högström, H. Bergström, and A. Rutgersson, 1999: A case study of air-sea interaction during swell conditions. *J. Geophys. Res.*, **104**, 25 833–25 851, <https://doi.org/10.1029/1999JC900213>.
- Smedman, A., U. Högström, E. Sahleé, W. M. Drennan, K. K. Kahma, H. Pettersson, and F. Zhang, 2009: Observational study of marine atmospheric boundary layer characteristics during swell. *J. Atmos. Sci.*, **66**, 2747–2763, <https://doi.org/10.1175/2009JAS2952.1>.
- Sullivan, P. P., and E. G. Patton, 2011: The effect of mesh resolution on convective boundary layer statistics and structures generated by large-eddy simulation. *J. Atmos. Sci.*, **68**, 2395–2415, <https://doi.org/10.1175/JAS-D-10-05010.1>.
- , C.-H. Moeng, B. Stevens, D. H. Lenschow, and S. D. Mayor, 1998: Structure of the entrainment zone capping the convective atmospheric boundary layer. *J. Atmos. Sci.*, **55**, 3042–3064, [https://doi.org/10.1175/1520-0469\(1998\)055<3042:SOTEZC>2.0.CO;2](https://doi.org/10.1175/1520-0469(1998)055<3042:SOTEZC>2.0.CO;2).
- , J. B. Edson, T. Hristov, and J. C. McWilliams, 2008: Large-eddy simulations and observations of atmospheric marine boundary layers above nonequilibrium surface waves. *J. Atmos. Sci.*, **65**, 1225–1245, <https://doi.org/10.1175/2007JAS2427.1>.
- , J. C. McWilliams, and E. G. Patton, 2014: Large-eddy simulation of marine atmospheric boundary layers above a spectrum of moving waves. *J. Atmos. Sci.*, **71**, 4001–4027, <https://doi.org/10.1175/JAS-D-14-0095.1>.
- Tambke, J., M. Lange, U. Focken, J.-O. Wolff, and J. A. T. Bye, 2005: Forecasting offshore wind speeds above the North Sea. *Wind Energy*, **8**, 3–16, <https://doi.org/10.1002/we.140>.
- Taylor, P. K., and M. J. Yelland, 2001: The dependence of sea surface roughness on the height and steepness of the waves. *J. Phys. Oceanogr.*, **31**, 572–590, [https://doi.org/10.1175/1520-0485\(2001\)031<0572:TDOSSR>2.0.CO;2](https://doi.org/10.1175/1520-0485(2001)031<0572:TDOSSR>2.0.CO;2).
- Thomas, P. D., and C. K. Lombard, 1979: Geometric conservation law and its application to flow computations on moving grids. *AIAA J.*, **17**, 1030–1037, <https://doi.org/10.2514/3.61273>.
- Toba, Y., S. D. Smith, and N. Ebuchi, 2001: Historical drag expressions. *Wind Stress over the Ocean*, I. S. F. Jones and Y. Toba, Eds., Cambridge University Press, 35–53.
- WAVEWATCH III Development Group, 2016: User manual and system documentation of WAVEWATCH III. Tech. rep., NOAA/NWS/NCEP/MMAB, 326 pp., <http://polar.ncep.noaa.gov/waves/wavewatch/manual.v5.16.pdf>.
- Westerhellweg, A., B. Canadillas, A. Beeken, and T. Neumann, 2010: One year of lidar measurements at FINO1-platform: Comparison and verification to met-mast data. *10th German Wind Energy Conf. DEWEK 2010*, Bremen, Germany, DEWI GmbH/Deutsches Windenergie-Institut, 5 pp., https://www.dewi.de/dewi/fileadmin/pdf/publications/Publikations/S01_3.pdf.
- , T. Neumann, and V. Riedel, 2012: FINO1 mast correction. *DEWI Magazin*, No. 40, DEWI, Wilhelmshaven, Germany, 60–66, https://www.dewi.de/dewi/fileadmin/pdf/publications/Magazin_40/09.pdf.
- Yang, D., C. Meneveau, and L. Shen, 2013: Dynamic modelling of sea-surface roughness for large-eddy simulation of wind over ocean wavefield. *J. Fluid Mech.*, **726**, 62–99, <https://doi.org/10.1017/jfm.2013.215>.